Chapter 4
Bifunctional Nanomaterials: Magnetism, Luminescence and Multimodal Biomedical Applications

Latif U. Khan and Zahid U. Khan

Abbreviations

AA	Acrylic acid
AC	Alternating current
Acac	Acetylacetone
B.M.	Bohr magneton
Calix	Calixarene
CNT	Carbon nanotube
CPE	Carbon-paste electrode
CS	Chitosan
CT	Computed tomography
CTAB	Cetyltrimethyl-ammonium bromide
Cup	*N*-nitrosophenylhydroxylamine
DNA	Deoxyribonucleic acid
DTAB	Dodecyltrimethylammonium bromide
FI	Fluorescent imaging
FITC	Fluorescein isothiocyanate
GO	Graphene oxide
IgG	Immunoglobulin G

L.U. Khan (✉)
Brazilian Nanotechnology National Laboratory (LNNano), Brazilian Center for Research in Energy and Materials (CNPEM), Rua Giuseppe Máximo Scolfaro, 10.000 Polo II de Alta Tecnologia de Campinas - CEP 13083-970, Campinas, São Paulo, Brazil.
e-mail: latif.khan@lnnano.cnpem.br

Z.U. Khan
Departamento de Imunologia, Instituto de Ciências Biomédicas-IV, Universidade de São Paulo, Av. Lineu Prestes, 1730, 05508-000, São Paulo, SP, Brazil
e-mail: zahidkhan@usp.br

S.K. Sharma (ed.), *Complex Magnetic Nanostructures*,
DOI 10.1007/978-3-319-52087-2_4

IUPAC	International Union of Pure and Applied Chemistry
IVCT	Intervalence charge transfer
LBL	Layer-by-layer
mcDNA	Minicircle DNA
MNPs	Magnetic nanoparticles
MRI	Magnetic resonance imaging
MRT	Magnetic resonance tomography
MTT	Microculture tetrazolium assay
MWCNT	Multiwalled carbon nanotube
NADH	Nicotinamide adenine dinucleotide
NIR	Near-infrared
NIPAM	*N*-isopropylacrylamide
OA	Oleic acid
o/w	Oil dispersed in water
PAH	Poly(allylamine hydrochloride)
PCEM	Point charge electrostatic model
PCL	Poly(ε-caprolactone)
PEG	Polyethylene glycol
PET	Positron emission tomography
Phen	1,10-phenanthroline
PLGA	Poly(lactic-*co*-glycolic acid)
PMAA	Poly(methacrylic acid)
PMI	*N*-(2,6-diisopropylphenyl)-perylene-3,4-dicarbonacidimide
PS	Polystyrene
PSS	Poly(styrenesulfonate)
PVP	Poly(vinylpyrrolidone)
QD	Quantum dot
rGO	Reduced graphene oxide
SAR	Specific absorption rate
siRNA	Small interfering RNA
SLPC	Specific losses per cycle
SPECT	Single-photon emission computed tomography
St	Styrene
TEOS	Tetraethyl orthosilicate
UCNPs	Upconversion luminescent nanoparticles
w/o	Water dispersed in oil

4.1 Introduction

Bifunctional nanosized materials, coassembling magnetic and photonic features into single-entity nanostructures [1, 2], have demonstrated great potential in wide range of multimodal biomedical applications, for example, as drug delivery carriers [3], in the photothermal destruction of tumor cells [4], as multimodal MRI contrast agents [5], in quantitative DNA analyses [6], and in magnetic hyperthermia for cancer

therapies [7–9]. Several reports have focused on the preparation, characterization, and biological applications of bifunctional optical and magnetic nanomaterials. Generally, these nanoscale materials can be obtained by coating or layer-by-layer (LBL) deposition of rare-earth phosphors [3, 10] quantum dots (QDs) [11] on magnetic core nanoparticles, polymer-assisted encapsulation or coassembly of magnetic nanoparticles and luminophores in single nanostructures [12], and functionalization of Fe_3O_4 with fluorescent dyes [13] or luminescent metal complexes [14].

Magnetite crystallizes in inverse spinel structures with Fe^{2+} and Fe^{3+} ion distribution, represented by the structural formula $(Fe^{3+})[Fe^{3+}Fe^{2+}]O_4$, where the parentheses denote tetrahedral (*A*) sites and the square brackets denote octahedral [*B*] sites [15]. Fe_3O_4 can be modified by the introduction of d transition-metal cations into its structure, such as Co^{2+}, Ni^{2+}, Cu^{2+}, Mn^{2+}, and Zn^{2+}. These modified ferrospinels are commonly known as ferrites, an important class of iron oxides with the general formula MFe_2O_4 [16–18]. Ferrites show a spinel-type structure in which oxygen (O^{2-}) ions form a face-centered cubic (fcc) close packing and the M^{2+} and Fe^{3+} ions occupy either tetrahedral (*A*) or octahedral (*B*) interstitial sites.

The intriguing structural feature has been obtained in ferrites by changing the scale of the particle size. When the materials are prepared in the microscopic range, they present an inverse spinel structure $(Fe)[MFe]O_4$, where () and [] mean *A* and *B* sites, respectively [19, 20]. However, in the nanometric range, they present a mixed-spinel structure $(Fe_{1-x}M_x)[Fe_{1+x}M_{1-x}]O_4$ $(0 < x < 1)$, where x is the so-called inversion degree [19], which indicates the cation distribution in the spinel structure.

The electronic structure of magnetic MFe_2O_4 ferrites shows only 3d energy states of metal ions near the Fermi level [21], so that optical absorption due to electric dipole–induced transitions is not expected at optical frequencies (parity forbidden) [22]. However, the diagonal components of the dielectric tensors of these compounds obtained by optical measurements show strong absorption bands in the visible range. They are attributable to d–d intervalence charge transfer (IVCT) transitions in which a d electron of an M^{2+} ion is transferred to a neighboring Fe^{3+} ion, residing at octahedral sites, through optical excitation [21, 22]. This charge transfer cannot occur between cations at octahedral and tetrahedral sites because the change in geometry between the two sites is too great. A similar cation-to-cation charge transfer is responsible for the color of the black mineral magnetite or lodestone [23].

In addition, like ferric oxide (hematite, α-Fe_2O_3) and various Fe^{3+} ions containing iron oxide, hydroxides give many soils and rocks a ruddy color. At the simplest level, the color derives from O^{2-} or $^{-}OH \rightarrow Fe^{3+}$ charge transfer because Fe^{3+} (d^5) ions readily accept extra electrons in their half-filled shells to become Fe^{2+} (d^6) ions [23]. Therefore, iron oxides are usually strong luminescence quenchers [24]. This phenomenon occurs via an energy transfer process when a luminescent center (e.g., RE^{3+} ion) is in direct contact with or is in proximity to a magnetic metal oxide surface (e.g., Fe_3O_4). To overcome this difficulty, an intermediate layer or spacer is usually added to separate iron oxide nanoparticles and luminophores [1, 12]. Therefore, magnetic ferrite nanoparticles are coated with, for example, organic

macrocycles, polymers, or silica before the introduction of a luminophore (e.g., rare-earth phosphor) to prepare the luminescent and magnetic nanomaterials.

Interest in luminescent materials containing RE^{3+} ions has grown considerably owing to their unique ability to exhibit well-defined narrow emission bands in different spectral ranges from visible to near-infrared (NIR) with relatively long lifetimes and high quantum yields [25, 26]. These characters make RE^{3+} materials efficient candidates for multidisciplinary photonic applications [27], recently extended from laser physics to, for example, materials sciences, optical markers, agriculture, and medical diagnostics.

The photoluminescence properties of RE^{3+} ions are mainly due to the 4f energy level structures [28], which are only slightly affected by the chemical environment owing to the effective shielding of 4f electrons by external filled 5s and 5p subshells [25]. Therefore, the absorption and emission spectra of the 4f intraconfigurational transitions of RE^{3+} ions retain more or less their atomic character and show similar absorption and emission lines irrespective of the host matrix or organic ligand [1, 29]. Rare-earth complexes have become valuable candidates for light conversion molecular devices (LCMDs) since the introduction of intramolecular energy transfer from organic ligands to RE^{3+} ions (*antenna effect*) [30] and after the issue of very low molar absorption coefficients (1.0 M^{-1} cm^{-1}) [29] of 4f–4f transitions was overcome. Therefore, the designs of efficient luminescent RE^{3+} complexes have become an important research subject [31] and are being investigated extensively using different organic ligands as sensitizers [32].

RE^{3+} ions are paramagnetic owing to the presence of unpaired electrons, with the exception of La^{3+}, Lu^{3+}, and Y^{3+}. Their magnetic properties are determined entirely by the ground state (except for Sm^{3+} and Eu^{3+} ions) because the excited states are so well separated from the ground state owing to the spin–orbit coupling and are thermally inaccessible [33]. The magnetic moment of RE^{3+} ions is essentially independent of the chemical environment, and one cannot distinguish between different coordination geometries. However, the magnetic moments of rare-earth ions [1] also contribute to the total magnetization of luminescent and magnetic nanomaterials. This chapter presents a concise overview of the key concepts of various strategies to fabricate bifunctional nanomaterials and their magnetism and photoluminescence behaviors, as well as their multimodal biomedical applications.

4.2 Strategies for Designing Bifunctional Nanomaterials

Luminescent and magnetic nanomaterials are usually fabricated by integrating magnetic nanoparticles with luminophores (e.g., RE^{3+} ion–doped compounds) by various synthetic methods. These materials are commonly achieved as hybrid conjugates of magnetic and luminescent entities or core-shell nanostructures, which are obtained by coating or LBL deposition of rare-earth phosphors and QDs on magnetic core nanoparticles. The other interesting way is the functionalization of magnetic iron oxide nanoparticles with fluorescent dyes and luminescent

complexes. For the sake of understanding, the strategies of preparation of bifunctional nanomaterials are divided into two parts, the synthesis of magnetic core nanoparticles and synthesis of bifunctional luminescent and magnetic nanomaterials.

4.2.1 Synthesis of Magnetic Core Nanoparticles

Magnetic nanoparticles (MNPs) are of various chemical compositions, crystalline structures, and phases, for example, iron oxides: Fe_3O_4, γ-Fe_2O_3, and α-Fe_2O_3 [34–38]; spinel-type ferrites: MFe_2O_4 (M^{2+}: Co, Mg, Mn, and Zn) [15–18, 21, 22]; pure metals: Fe and Co [39–41]; and alloys: $CoPt_3$ and FePt [42, 43]. Remarkable advances in chemical methods of synthesis have allowed for the preparation of MNPs with relatively narrow size distributions, good chemical stabilities, and a broad range of compositions, specific shapes, and morphologies. Several popular methods, including coprecipitation, thermal decomposition, hydrothermal synthesis, microemulsion, sol-gel synthesis, sonochemical reaction, flow injection synthesis, electrospray synthesis, and laser pyrolysis techniques, are used to synthesize high-quality MNPs [15, 44–46]. However, the most common methods for the preparation of MNPs are chemical coprecipitation, thermal decomposition, microemulsion, and hydrothermal synthesis. In this connection, we explain typical and representative examples of each synthetic process with the corresponding formation mechanism.

4.2.1.1 Coprecipitation

Generally, coprecipitation can be defined as "the simultaneous precipitation of more than one substance from a homogeneous solution," which results in the formation of a crystalline structure of a single phase (e.g., Fe_3O_4). Coprecipitation is probably the most convenient and efficient chemical pathway to synthesize MNPs. Iron oxides (either Fe_3O_4 or γ-Fe_2O_3) are usually prepared from a stoichiometric mixture of aqueous Fe^{2+}/Fe^{3+} salt solutions by the addition of a base, such as $NH_3{\cdot}H_2O$ or NaOH, under an inert atmosphere at room or elevated temperatures. The chemical reaction of Fe_3O_4 formation may be represented by Eq. 4.1:

$$Fe^{2+} + 2Fe^{3+} + 8OH^- \rightarrow Fe_3O_4 + 4H_2O \tag{4.1}$$

Thermodynamically, the complete coprecipitation of Fe_3O_4 is expected at a pH between 8 and 14 in inert atmosphere [15, 47]. However, owing to its sensitivity to oxidation, magnetite (Fe_3O_4) is usually transformed into maghemite (γ-Fe_2O_3) in the presence of oxygen:

$$Fe_3O_4 + 2H^+ \rightarrow \gamma\text{-}Fe_2O_3 + Fe^{2+} + H_2O. \quad (4.2)$$

Oxidation in air is not the only way to change magnetite (Fe_3O_4) into maghemite (γ-Fe_2O_3). However, the pH of the suspension is also affected by Fe_3O_4, as shown by Eq. 4.2, under acidic and anaerobic conditions, and surface Fe^{2+} ions are desorbed as hexaaqua complexes in solution [15, 47]. Therefore, acidic solutions usually cause the dissolution of magnetite.

Coprecipitation is a very convenient and favorable way to prepare a broad range of nanomaterials of various chemical compositions owing to the relatively mild reaction conditions, low cost of required equipment, simple protocols, and short reaction time. Therefore, this method is not only a preferred way to synthesize magnetic iron oxide nanoparticles but is also commonly used to prepare a wide range of rare-earth ion (RE^{3+})–doped luminescent nanomaterials, such as rare earth ion (RE^{3+})–doped alkaline-earth tungstates: MWO_4:RE^{3+} (M^{2+}: Ca, Sr, and Ba) [48], rare-earth fluorides: $NaYF_4$:RE^{3+} [49], LaF_3:RE^{3+} [50], and others. The great advantage of the coprecipitation method is that it yields a large amount of nanoparticles. However, polydisperse and large size distribution particles are usually obtained with this method owing to the kinetic factors that control the growth of crystals. Generally, two processes are involved in the growth and formation of particles [15, 45, 51, 52]: a rapid nucleation (aggregation of nanometric building blocks such as prenucleation clusters), which occurs when the concentration of species reaches critical supersaturation, and the slow growth of nuclei by the diffusion of solutes to crystal surfaces. Therefore, to produce monodisperse iron oxide nanoparticles, control of these processes is important. In a supersaturated solution when nuclei form at the same time, the subsequent growth of these nuclei results in the formation of particles with a very narrow size distribution [15].

Magnetic properties, such as saturation magnetization, coercive field, and blocking temperature, also depend on particle size, and a large particle size distribution results in a wide range of blocking temperatures [53]. The variety of factors should be adjusted to control the size, shape, magnetic characteristics, and other features of iron oxide nanoparticles. The control of the size, shape, and composition of MNPs depends on the type of iron salts used (e.g., chlorides, sulfates, nitrates, perchlorates), Fe^{2+}/Fe^{3+} ratio [15, 45], air or inert atmosphere, reaction rate, and temperature [54]. Kim and coworkers [55] reported that the synthesis of magnetite under continuous nitrogen gas flow not only protects critical oxidation but also reduces the particle size when compared with coprecipitation methods that do not involve the removal of oxygen. In this regard, the particle size is reduced from 8.0 nm (air atmosphere) to 6.0 nm (nitrogen atmosphere). The particle size also depends on the pH and ionic strength of the precipitation medium. It has been reported that by controlling the pH and ionic strength imposed by noncomplexing salt (e.g., $NaNO_3$) in the medium, the particle size decreases with increasing pH and

ionic strength. Above a critical pH value, which depends on the ionic strength and temperature, secondary particle growth by Ostwald ripening no longer takes place [15, 56]. The stabilization of nanoparticles seems to result from thermodynamics rather than kinetics. Recently, significant advances have been made in the use of organic additives such as chelating organic acids (citric, gluconic, and oleic acids) and polymer surface complexing agents (e.g., dextran, carboxydextran, starch, polyvinyl alcohol, calixarenes) in coprecipitaion syntheses of iron oxide nanoparticles [45]. These organic additives stabilize nanoparticles in situ during growth and control their size.

4.2.1.2 Thermal Decomposition

The thermal decomposition method can be simply described as the decomposition of organometallic compounds (e.g., iron acetylacetonate) at high refluxing temperatures in high-boiling-point organic solvents (e.g., diphenyl ether) containing stabilizing surfactants (e.g., oleic acid and oleylamine). The most commonly used organometallic compounds are metal acetylacetonates [$M(acac)_n$], where M: Fe, Mn, Co, Ni, Cr, and $n = 2$ or 3 [57], cupferronates (M_xCup_x), where cup: *N*-nitrosophenylhydroxylamine ($C_6H_5N(NO)O^-$) [58], carbonyls, for example, iron pentacarbonyl [$Fe(CO)_5$], and others. [41]. Fatty acids, oleic acid, oleylamine, and hexadecylamine are more often used as surfactants. In addition, diphenyl ether, diethylene glycol, octylamine, octyl ether, hexadecanediol, octadecene, 1-hexadecene, and 1-octadecene are high-boiling-point organic solvents that are usually used in this method [15, 45, 57, 59]. It is noteworthy that the ratios of the starting materials, such as organometallic precursors, surfactants, and solvents, are the important parameters for controlling the size and morphology of MNPs. In addition, the reaction temperature, reaction time, and aging period may also be crucial for the efficient control of size and morphology [45].

The apparatus used for the preparation of nanoparticles by thermal decomposition can be easily designed synthetically in a laboratory (Fig. 4.1). It consists of a three-necked, round-bottom flask mounted on a heating/stirring plate and equipped with a glass water condenser. The temperature can be also monitored with a thermometer immersed in silicon oil's beaker, which is mounted on the heating/stirring plate. The inert atmosphere in the reaction medium can be maintained by the continuous flow of nitrogen or argon gas during the entire period of reaction.

Thermal decomposition is an efficient chemical method that is usually used to synthesize monodisperse MNPs with high crystallinity, controlled shape, and a narrow size distribution. A wide variety of MNPs can be prepared by this method, including magnetic metal oxides (e.g., Cr_2O_3, MnO, Co_3O_4, NiO, iron

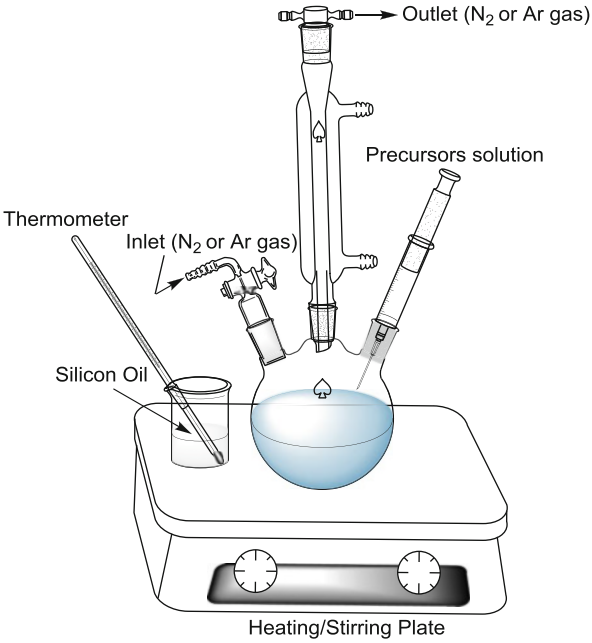

Fig. 4.1 Schematic illustration of apparatus used in synthesis of nanoparticles by thermal decomposition method (designed by author)

oxides ferrites), metallic nanoparticles (Fe, Ni, Co), and alloys ($CoPt_3$, FePt) [15, 39–41, 43, 45, 57, 58]. In addition, this chemical method has been used very commonly to prepare high-quality, various narrow-size-distribution rare earth ion–doped luminescent nanoparticles [60] such as $LiYF_4:RE^{3+}$ [61], $NaYF_4:RE^{3+}$ [62], $NaGdF_4:RE^{3+}$ [63], $NaLuF_4:RE^{3+}$ [64], $BaYF_5:RE^{3+}$ [65], $KY_3F_{10}:RE^{3+}$ [65], $BaGdF_5:RE^{3+}$ [66], $YOF:RE^{3+}$ [67], LaOF, and LuOF [68].

The advantage of metallic nanoparticles is their larger magnetization compared to metal oxides. Therefore, they are interesting candidates for data-storage devices. The precursors, which contain a zero-valence metal, such as metal carbonyls, usually undergo thermal decomposition and initially produce metal particles, but subsequent oxidation can lead to the formation of oxide nanoparticles as well. For instance, iron pentacarbonyl has been reported to decompose in a mixture of octyl ether and oleic acid at 100 °C, but subsequent addition of trimethylamine oxide $(CH_3)_3NO$ as a mild oxidant at high temperature results in the formation of monodisperse γ-Fe_2O_3 nanocrystals. Metallic iron nanoparticles have also been synthesized by thermal decomposition of $[Fe(CO)_5]$ at high temperature (170 °C) in the presence of polyisobutene (polymeric surfactant) and decalin (decahydronaphthalene) solvent in a nitrogen atmosphere [45]. Moreover, organometallic precursors with cationic metal centers usually undergo thermal decomposition to directly produce metal oxide particles. Rockenberger and coworkers [58] reported the formation of γ-Fe_2O_3, Mn_3O_4, and Cu_2O particles by the thermal decomposition of $FeCup_3$, $MnCup_2$, and $CuCup_2$ as precursors, respectively. Sun and coworkers [69] reported the size-controlled synthesis of magnetite nanoparticles at high temperature

(265 °C) using iron (III) acetylacetonate $Fe(acac)_3$ as precursor, in phenyl ether in the presence of alcohol, oleic acid, and oleylamine. Recently, compact $Ag@Fe_3O_4$ core-shell nanoparticles were synthesized by a temperature-paused single-step thermal decomposition method [70]. These nanoparticles showed a silver nucleus wrapped in a compact magnetite shell. Therefore, owing to the curious rectangular shape, they were represented as bricklike nanoparticles (BLNs). The interesting feature of this synthesis lies in the introduction of a temperature pause in the single-step protocol to separate the growth of silver (zone 1) from the proper thermal decomposition of the iron precursor (zone 2) (Fig. 4.2) and to avoid the formation of nonhomogeneous core-shell NPs.

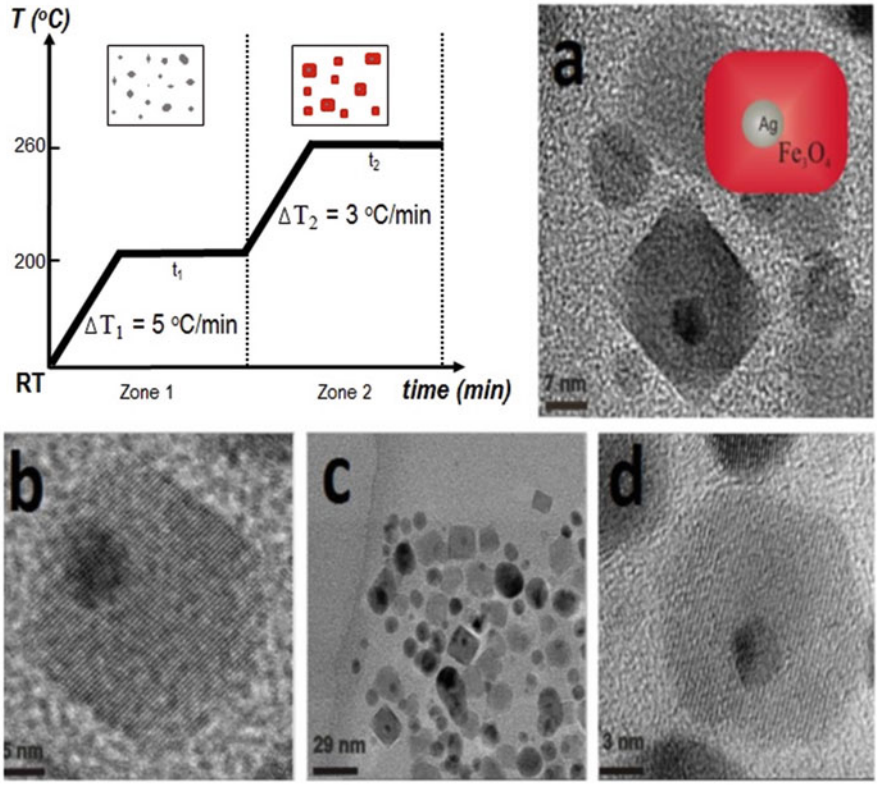

Fig. 4.2 Temperature profile of temperature-paused single-step thermal decomposition synthesis. *Boxes* sketch the expected predominant structures for each time zone. Typically, both waiting times are 120 min. Images: TEM images of BLNs obtained following the temperature-paused single-step protocol. Ag corresponds to a dark contrast, while lighter particles correspond to magnetite. Plain magnetite nanoparticles that form are also shown in (**c**). (**a**, **b**, **d**) Different amplifications of BLNs to understand the structure. Reproduced with permission from ref. [70]

4.2.1.3 Microemulsion

Microemulsion is a phenomenon that arises when two immiscible liquids (e.g., water and oil) are mixed together, and then a surfactant is added that stabilizes the dispersion of one of the phases (e.g., aqueous phase) in the other (e.g., organic phase). Surfactants are amphiphilic molecules that contain two well-differentiated hydrophobic and hydrophilic parts. They form a monolayer at the interface between the oil and water, with the hydrophobic tails of these molecules being dissolved in the oil phase and the hydrophilic head groups in the aqueous phase [71]. As a result, the surface tension between the two phases is reduced and the stable dispersion of one phase within the other is enabled through the formation of different structures, such as small drops, cylinders, and layers, depending on the mass relation between the aqueous and organic phases and surfactant [72]. Therefore, a microemulsion can be defined as a thermodynamically stable isotropic dispersion of two immiscible liquids (e.g., water and oil), where the microdomain of either or both liquids is stabilized by an interfacial film of surfactant molecules [45, 72]. In addition, Danielsson and coworker [73] defined a microemulsion as "a system of water, oil and amphiphile which is a single optically isotropic and thermodynamically stable liquid solution." Microemulsions are usually direct (oil dispersed in water, o/w) and reversed (water dispersed in oil, w/o). In the case of water-in-oil microemulsions, the aqueous phase is dispersed as microdroplets (usually 1–50 nm in diameter) surrounded by a monolayer of surfactant molecules in the continuous organic phase. The size of the reverse micelle is determined by the molar ratio of water to surfactant [45].

Micelles are aggregates of surfactant molecules dispersed in a liquid colloid (made of two immiscible liquids, e.g., water and oil). Like microemulsions, micelles can be normal-phase and reverse. Generally, micelles in aqueous solution form an aggregate with hydrophilic head parts in contact with surrounding solvent (water), and hydrophobic tail parts are extended in the micelle center (Fig. 4.3). These types

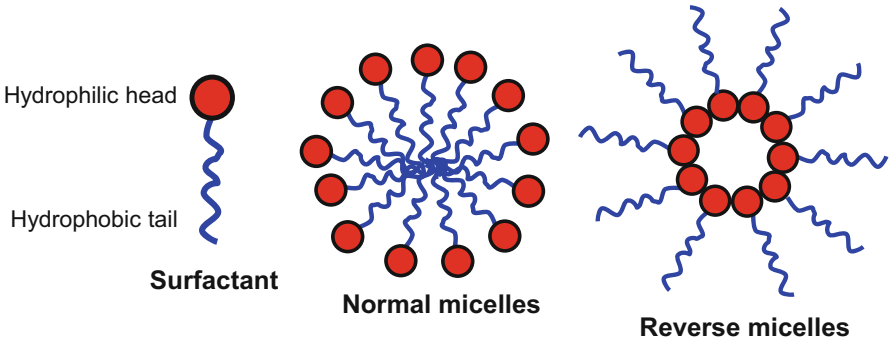

Fig. 4.3 Schematic representation of normal (*middle*) and reverse (*right*) micelles. Reproduced with permission from ref. [72]

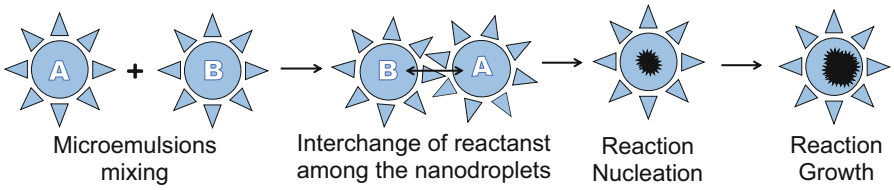

Fig. 4.4 Mechanism of formation of nanoparticles in microemulsions. Reproduced with permission from ref. [76]

of micelles are known as normal (oil-in-water) micelles [74]. Reverse micelles have head groups at the center with the tails extending out (water-in-oil micelle).

Micelles can be regarded as real nanoreactors, providing a suitable environment for controlled nucleation and growth. Therefore, microemulsion is a remarkable technique that provides very good control over the final particle size [45, 71, 74]. The mechanism of the microemulsion method is really simple and involves mixing two identical water-in-oil microemulsions containing appropriate reactants (e.g., A and B); the resulting microdroplets will continuously collide, coalesce, break up again, and interchange reactants, and finally a reaction will be occur to form a precipitate (nanoparticles) in the micelles (Fig. 4.4). By the addition of a solvent, such as acetone or ethanol, to a microemulsion, the precipitate can be extracted by filtering or centrifuging the mixture. In this regard, a microemulsion can be used as a nanoreactor for the formation of nanoparticles.

A water-in-oil microemulsion can be used to synthesize iron oxide, metallic iron nanoparticles, and silica-coated iron oxide nanoparticles employing several surfactants such as sodium dodecyl sulfate (SDS), cetyltrimethylammonium bromide (CTAB), and polyvinylpyrrolidone (PVP) [71]. The spinel MFe_2O_4 (M: Mn, Co, Ni, Cu, Zn, Mg, or Cd) ferrites are among the most important magnetic materials and have been widely used in electronic applications. Spinel ferrites can also be synthesized by microemulsions and reverse micelles. For instance, $MnFe_2O_4$ nanoparticles with controlled sizes from about 4–15 nm have been synthesized through the formation of water-in-toluene reverse micelles with sodium dodecylbenzenesulfonate (NaDBS) as surfactant [75]. In addition, Hashim and coworkers [76] reported the synthesis of manganese ferrite nanoparticles through the formation of water-in-cyclohexane reverse micelles, using cetyltrimethyl-ammonium bromide (CTAB) as surfactant and isoamylalcohol as the cosurfactant phase. In this synthesis, they schematically illustrated the preparation of $Mn^{3+}{}_xMn^{2+}Fe_{2-x}O_4$ ferrite nanoparticles by a reverse microemulsion method, as shown in Fig. 4.5, which is a remarkable representation of the synthesis of nanoparticles through the formation of reverse micelles and more easily understood by readers.

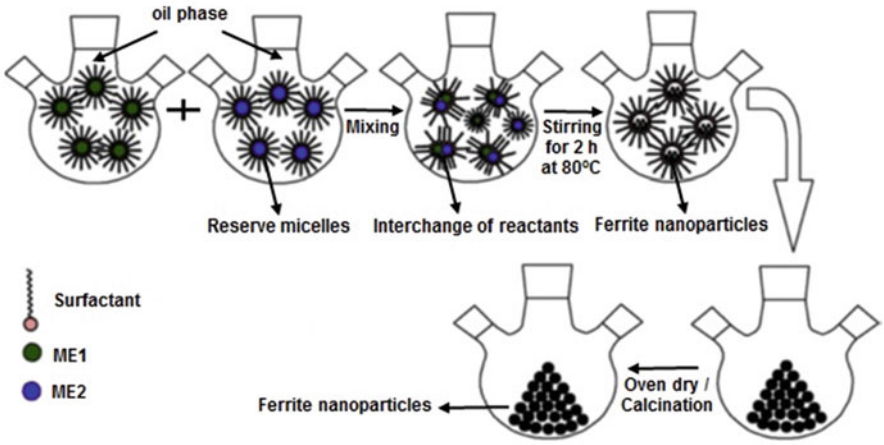

Fig. 4.5 Schematic representation of preparation of $Mn^{3+}{}_{x}Mn^{2+}Fe_{2-x}O_4$ ferrite synthesized by reverse microemulsion. Reproduced with permission from ref. [76]

4.2.1.4 Hydro(Solvo)Thermal Synthesis

Hydro(solvo) thermal synthesis usually refers to heterogeneous or homogeneous chemical reactions in water or nonaqueous media in an autoclave (a sealed thick-walled steel vessel with a Teflon cup) at high temperatures and high vapor pressure with subsequent growth of single crystals or crystallization of substances from the solution (e.g., aqueous solution). This method can be used to prepare different kinds of geometries, including thin films (e.g., nanostructured TiO_2 thin films) [77], bulk powders (e.g., zinc oxide powders) [78], single crystals (e.g., 3D metal–organic framework based on a lower-rim acid-functionalized calix[4]arene) [79], and nanocrystals (e.g., highly crystalline Fe_3O_4 nanoparticles) [80].

An excellent example of hydrothermal conditions is an aqueous medium over 100 °C and 1 bar pressure, which occurs in nature. Therefore, numerous minerals have been formed under these conditions. Through simulations in the laboratory, geologists and mineralogists have already been able to determine the conditions necessary for mineral formation and have thus contributed to the knowledge of geological processes [81]. Hydrothermal processes play an important role in industry, especially hydrometallurgy, for example, the classic Bayer process [81] for the decomposition of bauxite.

The material nature of the vessel (autoclave) should be chosen to be compatible with reaction media and conditions in hydrothermal synthesis. Therefore, the corrosive properties of the solution under the desired conditions as well as the danger of undesirable contamination of the reaction product must be considered. It has been found that certain metallic vessels, such as copper and nickel in particular, as well as titanium, vanadium, chromium, and iron, are attacked by alkaline solutions at 400 °C. Borosilicate and quartz glasses are quite stable toward neutral

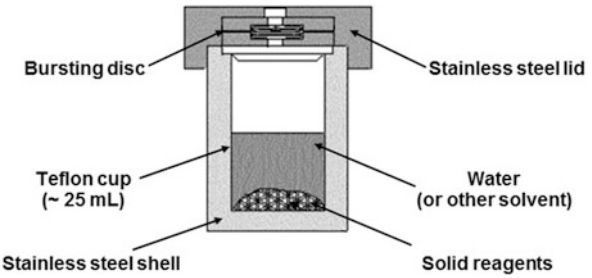

Fig. 4.6 Schematic of Teflon-lined stainless steel autoclave typically used in laboratories for hydrothermal synthesis. Reproduced with permission from ref. [82]

and acidic solutions, with the exception of hydrogen fluoride (HF) [81]. Therefore, in a neutral or acidic medium as well as within a limited pressure and temperature range, glass or quartz glasses are well suited for hydrothermal synthesis. In addition, Teflon is usually stable toward acids, even hydrogen fluoride, basic, and oxidizing media, but should be used within the temperature limit to avoid its melting. Thus, Teflon-lined stainless steel autoclave is the most common vessel [82] and is typically used in the laboratory for hydrothermal synthesis (Fig. 4.6).

A Teflon lining is important to avoid contamination from steel. As far as hydro(solvo)thermal synthesis in the laboratory is concerned, the filling factor of autoclave is important, and it should be sufficient to provide the necessary pressure, so filling factors of approximately 70% are normally used (i.e., 70% of the autoclave should be filled with reaction content). For most hydrothermal syntheses, only moderate temperatures between 100 and 250 °C are used, meaning that the hydrothermal conditions are below the supercritical region. Moreover, a minimum solubility of 2–5% is necessary for the least soluble reaction precursors [81, 82]. The autoclave is usually heated either by placing it in an oven or by using microwaves.

The specific reaction medium (solvent) and adjustment of reaction conditions, for example, temperature, pressure, and pH, are important for the preparation of specific materials using the solvothermal method. In the case of nanoparticles, the size, shape distribution, and crystallinity of the particles are precisely controlled by tuning the parameters, such as temperature, pressure, and reaction time. The solvent choice is not just limited to water; organic solvents, such as ethanol, can also be used in this method. Nevertheless, water remains the most widely used solvent. In addition, in hydro(solvo)thermal synthesis, some organic additives or surfactants with specific functional groups, for example, oleic acid (OA) [80], polyethylenimine (PEI) [83], and cetyltrimethylammonium bromide (CTAB), are generally added along with reaction precursors to achieve simultaneous control over the crystalline phases, sizes, and morphologies, as well as the surface functional groups, for the resulting nanoparticles.

The broad range of nanostructured materials can be synthesized by the hydro(solvo)thermal method, using optimized reaction conditions, for example, temperature, pressure, and pH. Li and coworkers [80] reported a generalized approach of the hydrothermal method for synthesizing a variety of different nanocrystals, for example, nanocrystals of metal (e.g., Ag, Au, Pd, Pt), magnetite

and spinel ferrites (e.g., MFe_2O_4, M^{2+}: Co, Mg, Mn, Zn), rare-earth fluorides (e.g., $NaYF_4$, YF_3, LaF_3) and semiconductors (e.g., CdS, ZnS, CdSe), by a liquid–solid solution reaction. This general hydrothermal approach consists of metal linoleate (solid), an ethanol–linoleic acid (liquid phase), and water–ethanol (solution) at different reaction temperatures under hydrothermal conditions. Later on the same method was applied by several authors to synthesize controlled size and morphology, highly crystalline Fe_3O_4 nanocrystals with a modification using different fatty acids, such as oleic acid and metal oleate solid precursor instead of linoleic acid and metal linoleate, and optimizing the hydrothermal parameters [3]. In this case the oleic acid acted as stabilizer to prevent particle agglomeration and to prevent the oxidation of Fe_3O_4 in air atmosphere.

Schüth and coworkers [45] summarized the four previously mentioned synthetic methods on the basis of their advantages and disadvantages in a convenient way (Table 4.1). Coprecipitation is usually considered the preferred route because of its simplicity of the synthesis. As far as the control of the size and morphology of nanoparticles is concerned, thermal decomposition seems like the best method developed to date. Alternatively, microemulsions can also be used to synthesize monodispersed nanoparticles with various morphologies. However, this method requires a large amount of solvent and the resulting yield of nanoparticles is comparatively low. Hydrothermal synthesis is a relatively little explored method for the synthesis of MNPs, although it allows for the synthesis of high-quality nanoparticles.

A literature review shows that MNPs prepared from coprecipitation and thermal decomposition methods have been extensively studied, and they can be prepared on a large scale. In addition, a broad range of particles of different chemical compositions, such as metals, luminescent rare-earth fluorides, rare earth–doped metal oxides, QDs, and semiconductors, can also be prepared by coprecipitation, thermal decomposition, and hydrothermal methods.

4.2.2 Synthesis of Luminescent and Magnetic Nanomaterials

Generally, the fabrication of luminescent and magnetic nanomaterials is categorized into three kinds of approaches. The first one is the preparation of optical and magnetic core-shell nanomaterials, based on coating or LBL deposition of rare-earth phosphors or QDs on the magnetic core nanoparticles. The second approach is based on combining luminophores and magnetic nanocrystals in single nanostructures assisted by crosslinking molecules. The third approach is the SiO_2-assisted synthesis of photoluminescent and magnetic nanomaterials using iron oxide as core nanoparticles and rare-earth-ion and transition-metal-ion complexes or fluorescent dyes as luminescent centers.

Table 4.1 Summary comparison of synthetic methods

Synthetic method	Synthesis	Reaction temp. [8 °C]	Reaction period	Solvent	Surface-capping agents	Size distribution	Shape control	Yield
Coprecipitation	Very simple, ambient conditions	20–90	Minutes–hours	Water	Needed, added during or after reaction	Relatively narrow	Not good	High/scalable
Thermal decom-position	Complicated, inert atmosphere	100–320	Hours–days	Organic compound	Needed, added during reaction	Very narrow	Very good	High/scalable
Microemulsion	Complicated, ambient conditions	20–50	Hours	Organic compound	Needed, added during reaction	Relatively narrow	Good	Low
Hydrothermal synthesis	Simple, high pressure	100–220	Hours-days	Water–ethanol	Needed, added during reaction	Very narrow	Very good	Medium

From [45] reproduced with permission

4.2.2.1 Optical and Magnetic Core-Shell Nanomaterials

Luminescent and magnetic core-shell nanomaterials are usually prepared by coating or LBL deposition of rare earth ion (RE^{3+})–doped compounds (e.g., $LaF_3:Ce^{3+},Tb^{3+}$, or $Y_2O_3:Eu^{3+}$) or QD (e.g., CdSe) shells on magnetic core nanoparticles (e.g., Fe_3O_4), using, for example, coprecipitation, thermal decomposition, or hydrothermal method, as discussed earlier in detail in Sects. 4.2.1.1, 4.2.1.2, and 4.2.1.4. Other interesting bifunctional nanostructures are based on the conjugation of QDs and MNPs. Several reports have focused on the preparation and characterization of these bifunctional nanomaterials. Zhang and coworkers [3] reported the stepwise synthesis of mesoporous multifunctional upconversion luminescent and magnetic nanorattles with controlled size and morphology for application in targeted chemotherapy (Fig. 4.7) and provided a good example of the fabrication of core-shell nanomaterials. Initially, they prepared $Fe_3O_4@SiO_2@Y_2O_3:Yb^{3+},Er^{3+}$ nanoparticles by thermal treatment of the $Fe_3O_4@SiO_2@Y(OH)CO_3{\cdot}H_2O:Yb^{3+},Er^{3+}$ precursor at 550 °C, which was obtained from Fe_3O_4/SiO_2 nanoparticles, $Y(NO_3)_3$, $Yb(NO_3)_3$, $Er(NO_3)_3$, and urea starting materials by the hydrothermal method. Furthermore, in the last step they treated the $Fe_3O_4@SiO_2@Y_2O_3:Yb^{3+},Er^{3+}$ nanomaterials with NaF and HF aqueous solutions at 80 °C to synthesize the $Fe_3O_4@SiO_2@\alpha$-$NaYF_4:Yb^{3+},Er^{3+}$ nanorattles through an ion-exchange process.

Tong and coworkers [84] have also studied luminescent and magnetic core-shell $Fe_3O_4@SiO_2@Y_2O_3:Eu^{3+}$ composites by annealing precursor material at 800 °C. The precursor was obtained from $Fe_3O_4@SiO_2$ nanoparticles, YCl_3, and $EuCl_3$ by

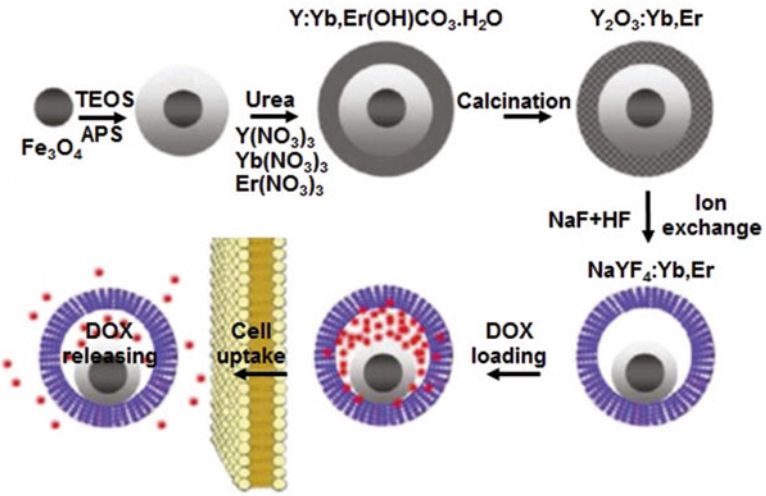

Fig. 4.7 Synthetic procedure for drug-loaded $Fe_3O_4@SiO_2@\alpha$-NaYF/Yb,Er nanorattles (DOX-MUC-F-NR). Reproduced with permission from ref. [3]

the hydrothermal method. The main disadvantage of annealing at high temperature (> 400 °C) is the oxidation of magnetite (Fe_3O_4) to hematite (α-Fe_2O_3), which greatly affects magnetic properties, causing a drastic decrease in the magnetization of the bifunctional nanomaterials. Moreover, owing to a sensitivity to oxidation, magnetite (Fe_3O_4) is usually transformed into maghemite (γ-Fe_2O_3) in the presence of oxygen, so magnetite core nanoparticles are stabilized with coating agents, for example, silica, organic compounds (e.g., oleic acid), or polymers, before use and an inert atmosphere is employed during the preparation of a luminescent shell (e.g., α-$NaYF_4$:Yb^{3+},Er^{3+}) on these nanoparticles. The pH of the reaction medium also affects the Fe_3O_4; under acidic and anaerobic conditions, surface Fe^{2+} ions are desorbed as hexaaqua complexes in solution. Therefore, acidic pH levels should be avoided during the synthesis of luminescent and magnetic core-shell nanomaterials.

Generally, core-shell optical and magnetic nanomaterials contain Fe_3O_4@$NaGdF_4$:Yb/Er@$NaGdF_4$:Yb/Er [85], Fe_3O_4@LaF_3:Yb^{3+},Er^{3+} [86], Fe_3O_4@YF_3:Ce^{3+},Tb^{3+} [87], and other compounds. (Table 4.2). In addition, various optical and magnetic nanostructures comprised of magnetic core nanoparticles and QDs as luminophores have been also extensively studied. These bifunctional nanomaterials include Fe_3O_4@CdSe [88], Fe_3O_4@C@CdTe [89], Fe_3O_4@ZnS [90], Co/CdSe [11], FePt@CdS, CdS-FePt [91], and other core-shell nanostructures and microspheres (Table 4.2).

Table 4.2 Summary of reported luminescent and magnetic core-shell nanomaterials

Magnetic species (core)	Luminophore (shell)	Method/conditions	Reference
Fe_3O_4	GdF_3:Er^{3+},Yb^{3+}	Coprecipitation	[92]
Fe_3O_4	Gd_2O_3:Eu^{3+}	Heating at 90 °C/calcination	[93]
Fe_3O_4	LaF_3:Ce^{3+},Tb^{3+}	Coprecipitation	[94]
Fe_3O_4	LaF_3:Yb^{3+},Er^{3+}	Coprecipitation/heating at 400 °C under N_2	[86]
Fe_3O_4	$NaGdF_4$: Yb^{3+},Er^{3+}	Thermolysis process	[85]
Fe_3O_4	α-$NaYF_4$:Yb^{3+},Er^{3+}	Hydrothermal/calcination/ion exchange	[3]
Fe_3O_4	YF_3:Ce^{3+},Tb^{3+}	Coprecipitation	[87]
Fe_3O_4	Y_2O_3:Eu^{3+}	Hydrothermal/calcination	[84]
Fe_3O_4	Y_2O_3:Tb^{3+}	Hydrothermal/calcination	[95]
Fe_3O_4	Y_2O_3:Yb^{3+},Er^{3+}	Heating/calcination under N_2	[96]
$FeYO_3$	Y_2O_3:Eu^{3+}	Hydrothermal/calcination/melamine/N_2	[97]
$CoFe_2O_4$	Y_2O_3:Eu^{3+}	Electrospinning technique/calcination	[98]
Fe_3O_4	YVO_4:Eu^{3+}	Coprecipitation	[99]
Fe_3O_4	CdSe	Thermal decomposition	[88]
Fe_3O_4	CdTe	Reduction using $NaBH_4$/heating	[100]
FePt	CdS	Thermal decomposition	[91]
Fe_3O_4	ZnS	Thermal decomposition	[101]

4.2.2.2 Crosslink-Assisted Synthesis of Luminescent and Magnetic Hybrid Nanostructures

A notable strategy to prepare bifunctional nanomaterials based on MNPs (e.g., Fe_3O_4) and luminescent compounds (e.g., $NaYF_4:Yb^{3+},Er^{3+}$) involves the use of crosslinking molecules, such as organic compounds, macrocycles (e.g., calixarene), and polymers (e.g., polyacrylic acid), which coassemble together the corresponding luminescent and magnetic entities into single nanostructures. The main difficulty in the combination of luminophores and MNPs is luminescence quenching, which occurs via an energy transfer process when a luminescent center (e.g., RE^{3+} ion) is in direct contact with or in proximity to a magnetic metal oxide surface (e.g., Fe_3O_4). To avoid this phenomenon, an intermediate layer or spacer is usually added to separate the MNPs and luminophores. Therefore, crosslinking molecules, such as organic macrocycles and polymers, may be good candidates for producing stable spacing layers between luminescent centers (e.g., RE^{3+} ions) and quenchers (e.g., Fe_3O_4) and also conjugating luminescent compounds with MNPs to produce bifunctional nanostructures. Several peer-reviewed articles have been published on these kinds of luminescent and magnetic nanomaterials, examining such aspects as their chemical synthesis and surface engineering for biomedical applications.

Yan and coworkers [102] reported superparamagnetic and upconversion emitting $Fe_3O_4/NaYF_4:Yb^{3+},Er^{3+}$ heteronanoparticles, prepared by a crosslinking–assisted strategy. In this synthesis, they used 1,10-decanedicarboxylic acid or 11-mercaptoundecanoic acid as crosslinkers to anchor the Fe_3O_4 nanoparticles onto the surface of $NaYF_4:Yb^{3+},Er^{3+}$ upconversion luminescent nanoparticles. Other interesting bifunctional nanoscale materials are green light–emitting superparamagnetic koosh nanoballs [103], which contain luminescent $LaPO_4:Ce^{3+}:Tb^{3+}$ and magnetic Fe_3O_4 nanoparticles assembled together by *p*-sulfonato-calix[6]arene macrocycle. Recently, Khan and coworkers [1] reported red-green–emitting and superparamagnetic nanomarkers based on Fe_3O_4 nanoparticles and rare-earth complexes conjugated together by *p*-tetrakis(carboxymethyl)calix-4-arene tetrol macrocycle (Fig. 4.8). In this work, the authors functionalized in situ Fe_3O_4 nanoparticles with *p*-tetrakis(carboxymethyl)calix-4-arene tetrol macrocycle via coprecipitation, then linked them to rare-earth complexes in one-pot syntheses.

Cheng and coworkers [4] described a novel class of multifunctional optical and magnetic nanomaterials based on upconversion luminescent $NaYF_4:Y^{3+}:Yb^{3+}:Er^{3+}$ and iron oxide nanoparticles. These nanomaterials are prepared by a LBL self-assembly procedure. In this procedure, ultrasmall superparamagnetic dopamine–modified iron oxide (Fe_3O_4) nanoparticles are adsorbed onto the surface of polyacrylic acid (crosslinking)–modified $NaYF_4:Y^{3+},Yb^{3+},Er^{3+}$ nanoparticles by electrostatic attraction to produce $NaYF_4:Y^{3+},Yb^{3+},Er^{3+}/Fe_3O_4$ nanostructures, and on top of which a thin gold shell is formed by seed-induced reduction growth.

Polymer-assisted assembly or encapsulation of MNPs and luminophores, for example fluorescent dyes or QDs, together into the same particles, on the basis of the methods used for the preparation of magnetic or fluorescent polymeric

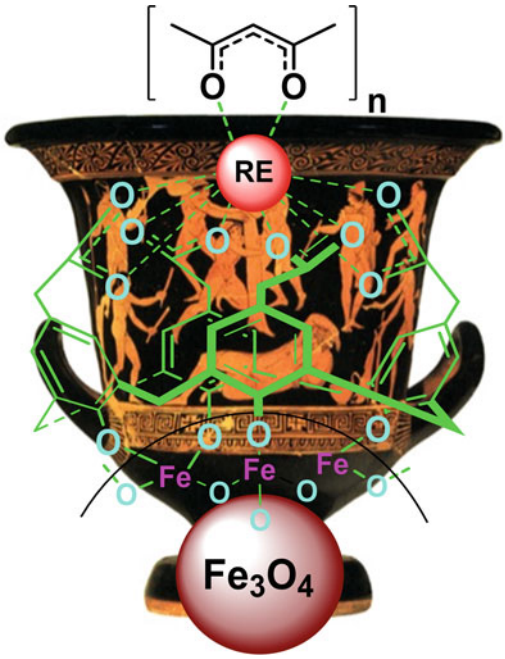

Fig. 4.8 Schematic illustration of structure of luminescent and magnetic nanoparticles containing Fe_3O_4 functionalized with RE^{3+} complex of β-diketonate and calixarene as ligands—Fe_3O_4@calix-RE(TTA or ACAC). Reproduced with permission from ref. [1]

particles, is widely used for the preparation of luminescent and magnetic nanomaterials. MNPs and fluorophores encapsulated together in nano- or micron-sized polymer particles can be fabricated by, for example, emulsion or miniemulsion polymerization, LBL self-assembly, solvent evaporation, or a microfluidic device for large-scale production (Table 4.3). Although the fluorescent and magnetic nanomaterials prepared by this concept can prevent MNPs from leaching into media and, consequently, maintain their magnetic properties, the luminescence quenching that occurs because of the close proximity of MNPs (quencher) to fluorophores is a serious concern. On the other hand, coating the polymer on single or aggregated magnetic core nanoparticles before introducing luminophores offers a promising solution to prevent the quenching effect.

Recently, Chen and coworkers [112] reported on a remarkable approach to coassemble MNPs with fluorescent QDs to form colloidal magnetofluorescent supernanoparticles. This strategy is based on combining CdSe-CdS core-shell QDs with Fe_3O_4 MNPs in the presence of dodecyltrimethylammonium bromide (DTAB) as a surfactant to produce QD-MNP micelles. Subsequent encapsulation of the QD-MNP micelles in PVP and ethylene glycol (EG) results in the formation of magnetofluorescent core-shell supernanoparticles. Additional thermal treatment transforms the randomly assembled Fe_3O_4 core nanoparticles into a periodic assembly with an fcc superlattice, producing magnetofluorescent core-shell supernanoparticles with a supercrystalline magnetic core.

Table 4.3 Bifunctional nanomaterials prepared by organic compound/polymer–assisted integration of luminophores with magnetic nanoparticles

Crosslinker (organic compound/polymer)	Magnetic species	Luminophore	Method	Reference
Calix	Fe_3O_4	$LaPO_4:Ce^{3+}:Tb^{3+}$	Coprecipitation/self-assembly process	[103]
Calix	Fe_3O_4	Eu^{3+} and Tb^{3+} complexes	Coprecipitation/RE^{3+} complex synthesis	[1]
1,10-Decanedicarb-oxylic acid or 11-mercaptoundecanoic acid,	Fe_3O_4	$NaYF_4:Yb^{3+},Er^{3+}$	Crosslink anchoring strategy	[102]
Poly(St-co-GMA)/Poly(St-NIPAM)	Fe_3O_4	Eu^{3+} complex ($Eu(AA)_3Phen$)	Two-step seed emulsifier–free emulsion polymerization technique	[104, 105]
PEG-diacid/polyethyleneglycol-bis-carboxymethyl ether	Fe_3O_4	$YPO_4:Eu^{3+}$	Covalent conjugation via amide bond formation	[106]
PEG	Fe_3O_4	$CaMoO_4:Eu^{3+}$	Encapsulation of $CaMoO_4$: Eu^{3+} and Fe_3O_4 in PEG by ultrasonication	[107]
Polyacrylic acid	Fe_3O_4	$NaYF_4:Y^{3+}:Yb^{3+}:Er^{3+}$	Polymer-assisted LBL deposition	[4]
PLGA	Fe_3O_4	Mn:ZnS QDs	Emulsion evaporation method	[108]
PSS and PAH	Fe_3O_4	CdTe QDs	LBL technique	[109, 110]
Commercial polymer having −SH and −COOH	γ-Fe_2O_3	CdSe/ZnS	Organic/water two-phase mixture	[111]

(continued)

Table 4.3 (continued)

Crosslinker (organic compound/polymer)	Magnetic species	Luminophore	Method	Reference
Polyvinylpyrrolidone/Ethylene glycol	Fe_3O_4	CdSe-CdS	Micelle process and encapsulation of QD-MNP micelles in PVP/EG	[112]
PS-co-AA	Fe_3O_4	PMI	Three-step miniemulsion process	[8]
PCL-b-PMAA	$MnFe_2O_4$	Pyrene	Nanoemulsion method	[113]
EG-diacrylate/PSSS/PAH	Fe_3O_4	Rhodamine B	Microfluidic device-based method/LBL	[114, 115]
PS	Janus magnetic emulsion	1-Pyrene carboxaldehyde	Swelling diffusion method	[116]
CS	γ-Fe_2O_3	FITC	Coating of FITC-CS onto γ-Fe_2O_3 surface	[117, 118]
P(HEMA)@P(NIPAAMco-AA)	Fe_3O_4	FITC	Combination of sol-gel, distillation precipitation polymerization (DPP), and RAFT polymerization process	[119]
PEG	$MnFe_2O_4$	1-Pyrene butyric acid	Self-assembly	[120]
Poly(styrene/divinylbenze-ne/acrylic acid) and CS	Fe_3O_4	FITC	Miniemulsion polymerization	[121]

4.2.2.3 SiO_2-Assisted Synthesis of Luminescent and Magnetic Nanomaterials

Silanization is a remarkable technique for the surface modification of MNPs that gives to nanoparticles biocompatibility and greater chemical and mechanical stability against variations in pH or temperature. The surface of a silica shell can be further functionalized with fluorescent dye molecules and also introduce specific ligand functional groups to graft with the luminescent metal complexes to produce multifunctional optical and magnetic nanomaterials.

Two essential methods for the coating of MNPs with silica are employed, acidic hydrolysis of silicate in aqueous solution and base-catalyzed hydrolysis of silicate (e.g., tetraethyl orthosilicate) in a mixture of organic solvent (e.g., ethanol) and water such as in a modified Stöber method [122]. In addition, a base-catalyzed silica coating of magnetic iron oxide nanoparticles was also reported by a water-in-cyclohexane microemulsion method, using a surfactant such as Triton X-100 [123], by which, generally, monodisperse uniform core-shell MNPs are obtained.

The silica coating of MNPs with the Stöber method is usually required in the pretreatment of these nanoparticles with small amounts of silicate in an aqueous solution in order to avoid their aggregation. Nevertheless, direct silica coating with TEOS in a mixture of ethanol and aqueous ammonia produces MNP clusters embedded in large silica aggregates. Moreover, the concentration of pretreated magnetic particles should be less than 12 mg L^{-1}; otherwise, large aggregates of nanoparticles may form.

Further detailed studies of coating nanoparticles with TEOS have revealed that this process is highly sensitive to experimental conditions such as ethanol/water ratio, concentration of ammonia and TEOS, and temperature. Silica coating using the Stöber method usually requires approximately 12–48 h of mechanical stirring at room temperature to obtain a uniform silica shell on the surface of MNPs. However, heating of the reaction mixture causes large MNP–silica aggregates with irregular morphology.

Recently, Pogorilyi and coworkers [124] reported that base-catalyzed silica coating by the Stöber method causes the oxidation of magnetite (Fe_3O_4) into maghemite (γ-Fe_2O_3). They observed that the larger the amount of TEOS used, the longer the reaction takes to complete, and so the deeper is the oxidation of the original magnetite phase, and in the end there will no longer be magnetite (Fe_3O_4), but predominantly maghemite (γ-Fe_2O_3). In addition, there is no visible transformation of magnetite into nonmagnetic hematite (α-Fe_2O_3), so the material remains strongly magnetic and effectively attracted to the magnet in dispersion and solid phases.

A variety of bifunctional optical and magnetic nanomaterials have been reported, on the basis of a modified Stöber method, using silica-coated magnetic iron oxide nanoparticles functionalized or grafted with luminescent rare-earth or transition-metal complexes and fluorescent dyes. Zhang and coworkers [125] reported the preparation of bifunctional nanocomposites by grafting a Tb^{3+} *N*-(4-benzoic acid-yl),*N*′-(propyltriethoxysilyl) urea) complex to SiO_2-coated Fe_3O_4 nanoparticles via

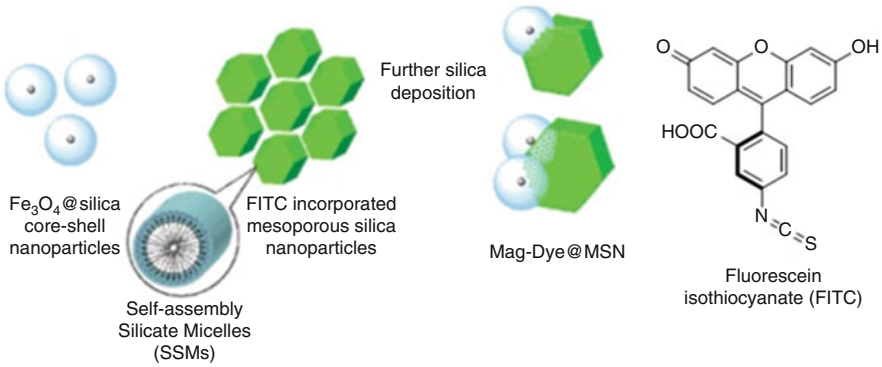

Fig. 4.9 Synthetic procedure of tumblerlike mesoporous silica nanocomposites (Mag-Dye@MSN). Reproduced with permission from ref. [13]

the Stöber method. Subsequently, Fu and coworkers extended the same method to produce Nd- and Yb-based luminescent (NIR) and magnetic nanocomposites using the same ligand and magnetic nanoparticles [126].

Mou and coworkers [13] prepared multifunctional nanocomposites, based on SiO_2-assisted assembly of fluorescent *N*-1-(3-trimethoxy-silylpropyl)-*N*-fluoresceyl thiourea (FITC-APTMS) with magnetic Fe_3O_4@SiO_2 nanoparticles through a self-assembled silicate micelle process (Fig. 4.9), using conditions similar to those of the Stöber method. In addition, bifunctional nanomaterials were reported by the encapsulation or incorporation of iron oxide nanoparticles and metal complexes [e.g., $Ru(bpy)_3Cl_2{\cdot}6H_2O$ complex] [14] in silica matrix through a modified Stöber or base-catalyzed microemulsion method.

4.3 Magnetism

By the 1930s, the magnetic characteristics of materials were extensively exploited owing to their key importance in some of the most significant inventions in modern technology, including magnetic sound recording and magnetic storage. Nothing was more representative of the modern world than the new marvels of radio and television, which incorporated magnetic components as important features of their design. The materials are usually either diamagnetic or paramagnetic and ferromagnetic. Diamagnetism is a phenomenon shown only by atoms that have no net magnetic moment as a result of their shells being filled or have all paired electrons classified as diamagnetic. On the other hand, diamagnetism is overshadowed by much stronger interactions such as paramagnetism and ferromagnetism, which occur in materials that have net magnetic moments due to the presence of unpaired electrons, giving them the classification as paramagnetic and ferromagnetic materials.

Remarkable advances in nanoscience and nanotechnology have led to a revolution in the research area of magnetism and applications of magnetic nanomaterials in different modern technologies having high efficiency. Common computer disks consist of granular magnetic materials, such as CoPtCr, with admixtures of boron or tantalum for recording and storing data. Recently, magnetic nanoscale materials have been widely explored to use in biomedical sciences, such as in drug delivery and the selective destruction of cancer cells through magnetic hyperthermia with photothermal support, still hot topics of research. Therefore, the scientific understanding of magnetism or the magnetic properties of materials remains rudimentary. Therefore, we attempt to explain simply the basic concept of magnetism in materials in a way that can be easily understood by nonspecialist readers.

4.3.1 Origin of Magnetism

Magnetism in materials is a consequence of *magnetic moments* associated with individual electrons. Moving electrons in atoms contain both an orbital magnetic moment $\mathbf{m}_l$, corresponding to their orbital angular momenta (**l**), and a spin magnetic moment $\mathbf{m}_s$, which is proportional to their spin angular momenta (**s**), as shown by Eqs. 4.3 and 4.4. To facilitate understanding, we establish a link between Ampère's ideas about circulating currents and the electronic structure of atoms. We can deduce that it is the angular momenta of electrons in atoms that correspond to Ampère's circulating currents and give rise to the magnetic dipole moment. In fact, the magnetic moment of a free atom in the absence of a magnetic field consists of *two* contributions. One is the motion of electrons in an orbit around the nucleus that give rise to their orbital angular momenta (**l**), and the other is the spin of electrons around their own axis, leading to their spin angular momenta (**s**). The spin and orbital angular momenta combine to produce the observed magnetic moment of atoms, which is measured in *Bohr magneton* (B.M.); consequently, each atom behaves like a tiny magnet:

$$\boldsymbol{m_l} = g_l \mathbf{l} \ \text{(B.M.)}\,, \tag{4.3}$$

$$\boldsymbol{m_S} = g_{SB} \mathbf{s} \ \text{(B.M.)}\,, \tag{4.4}$$

where g_l and g_S are orbital and spin *g-factors,* **s** is the *spin* of an electron, μ_B is *Bohr magneton* (9.274×10^{-24} J T^{-1}) and can be defined in terms of fundamental constants as $\mu_B = \text{B.M.} = \frac{eh}{4\pi mc}$, where e is the electron charge, h Planck's constant, m electron mass, and c the speed of light.

The magnetic moments of atoms, ions, and molecules are usually expressed in B.M., as explained earlier. In addition, the magnetic moment of a single electron is given according to wave mechanics by Eq. 4.5:

$$\mu_B \,(in \ \text{B.M.}) = g\sqrt{S\,(S+1)}, \tag{4.5}$$

where S is simply the absolute value of the spin quantum number (total spin of unpaired electrons in atom or ion) and g is the gyromagnetic ratio, more familiarly known as the g-factor; for a free electron its value is 2. This equation is also known as a "spin-only formula" [12]. The magnetic moment of transition elements is due to the presence of unpaired electrons, so the preceding Eq. 4.5 can be expressed as $\mu_{\text{spinonly}} = \sqrt{4S(S+1)}$ if only the entire spin of unpaired electrons is taken into account. In addition, it can also be related to the number of unpaired electrons n by the following Eq. 4.6:

$$\mu_{\text{spinonly}} = \sqrt{4S(S+1)} \approx \sqrt{n(n+2)}. \tag{4.6}$$

The orbital angular momentum of 3d transition metal ions is usually quenched by other surrounding ions in solid materials. This phenomenon is a consequence of the interaction of electric fields generated by surrounding ions with the 3d orbitals of metal ions restricting the orbital motion of the electrons. It is relevant that these electric fields cause the orbitals of metal ions to be coupled strongly to the crystal lattice, so that they are not able to reorient in response to an applied field and not contribute to the observed magnetic moment. On the other hand, the spins are only weakly coupled to the lattice, so they contribute to the magnetization process and, consequently, to the resultant magnetic moment of the material. In addition, if the orbital angular momentum makes a full contribution to the magnetic moment, then it can be calculated by Eq. 4.7:

$$\mu_{\text{LS}} = \sqrt{g^2 S(S+1) + L(L+1)} \approx g\sqrt{J(J+1)}. \tag{4.7}$$

Therefore, for first-row transition-metal ions in the periodic table, the measured magnetic moment is closer to the calculated one if the *orbital* angular momentum of the electrons is completely ignored. Table 4.4 lists the valuesof the measured and

Table 4.4 Calculated and measured effective magnetic moments for first-row transition-metal ions

Ion	Configuration	Fundamental level	$g\sqrt{J(J+1)}$	$g\sqrt{S(S+1)}$	m/μ_B
Ti^{3+}, V^{4+}	$3d^1$	$^2D_{3/2}$	1.55	1.73	1.8
V^{3+}	$3d^2$	$^3F_2$	1.63	2.83	2.8
Cr^{3+}, V^{2+}	$3d^3$	$^4F_{3/2}$	0.77	3.87	3.8
Mn^{3+}, Cr^{2+}	$3d^4$	$^5D_0$	0.00	4.90	4.9
Fe^{3+}, Mn^{2+}	$3d^5$	$^6S_{5/2}$	5.92	5.92	5.9
Fe^{2+}	$3d^6$	$^5D_4$	6.70	4.90	5.4
Co^{2+}	$3d^7$	$^4F_{9/2}$	6.63	3.87	4.8
Ni^{2+}	$3d^8$	$^3F_4$	5.59	2.83	3.2
Cu^{2+}	$3d^9$	$^2D_{5/2}$	3.55	1.73	1.9

From [127]. Reproduced with permission of John Wiley & Sons

calculated magnetic moments of 3d transition-metal ions using formulas considering the total angular momenta (J) and spin only. It is obvious that values calculated using a spin-only formula are in close agreement with experimental ones compared to values calculated using a formula taking into account the total angular momentum (J). This phenomenon is known as *quenching* of the orbital angular momentum, which is a consequence of the electric field generated by surrounding ions in solid materials. However, in rare-earth elements (from lanthanum to lutetium), there is no *quenching* of the orbital angular momentum, and hence both spin and orbital motions of 4f electrons contribute to the magnetic moment.

4.3.1.1 Magnetic Properties of Trivalent Rare-Earth Ions

Rare-earth ions are paramagnetic owing to the presence of unpaired electrons, with the exception of La^{3+}, Lu^{3+}, and Y^{3+} ions. The magnetic properties of rare-earth ions are determined entirely by the ground state (except for Sm^{3+} and Eu^{3+} ions) because their ground state is well separated by several hundred per centimeter from the next higher lying state (Fig. 4.10) owing to spin–orbit coupling and are thermally inaccessible. Unlike the d electrons of transition-metal ions, the 4f electrons of rare-earth ions are almost unaffected by the chemical environment, and 4f energy levels are the same as in free ions because of the very effective shielding by external filled $5s^2$ and $5p^6$ subshells. Consequently, rare-earth ions in compounds act in the same way as free ions, so their orbital angular momenta are not quenched by electric fields of the chemical environment, which effectively contributes to their magnetic moments (μ_{eff}).

Therefore, the magnetic moments of RE^{3+} ions are calculated in terms of the total angular momentum quantum number (J) by the use of HUND's formula (Eq. 4.8):

$$\mu_{\text{eff}} = g_j \sqrt{J\,(J+1)}, \tag{4.8}$$

where the Landé g-factor is defined by $g_J = \frac{S(S+1)+3J(J+1)-L(L+1)}{2J(J+1)}$.

The theoretical values of the magnetic moments of RE^{3+} ions, calculated with HUND's formula [128], are generally in good agreement with the experimental magnetic moments, with the exception of Sm^{3+} (f^5) and Eu^{3+} (f^6) ions, where the experimentally determined magnetic moments vary considerably with temperature. For these two ions the first excited J state is sufficiently close in energy to the ground state to be considerably populated at room temperature. Since these excited states have higher J values than the ground state, the actual magnetic moments are higher than those calculated by the use of Eq. 4.8 with the value of J for the ground state. Therefore, in the case of Sm^{3+} ions, the thermal population of the higher lying $^6H_{7/2}$ state leads to a magnetic moment of around $1.6\,\mu_B$, rather than $0.845\,\mu_B$, which would be expected if just the $^6H_{5/2}$ ground state were responsible (Table 4.5). Similarly, if the magnetic property of Eu^{3+} ions were determined solely by

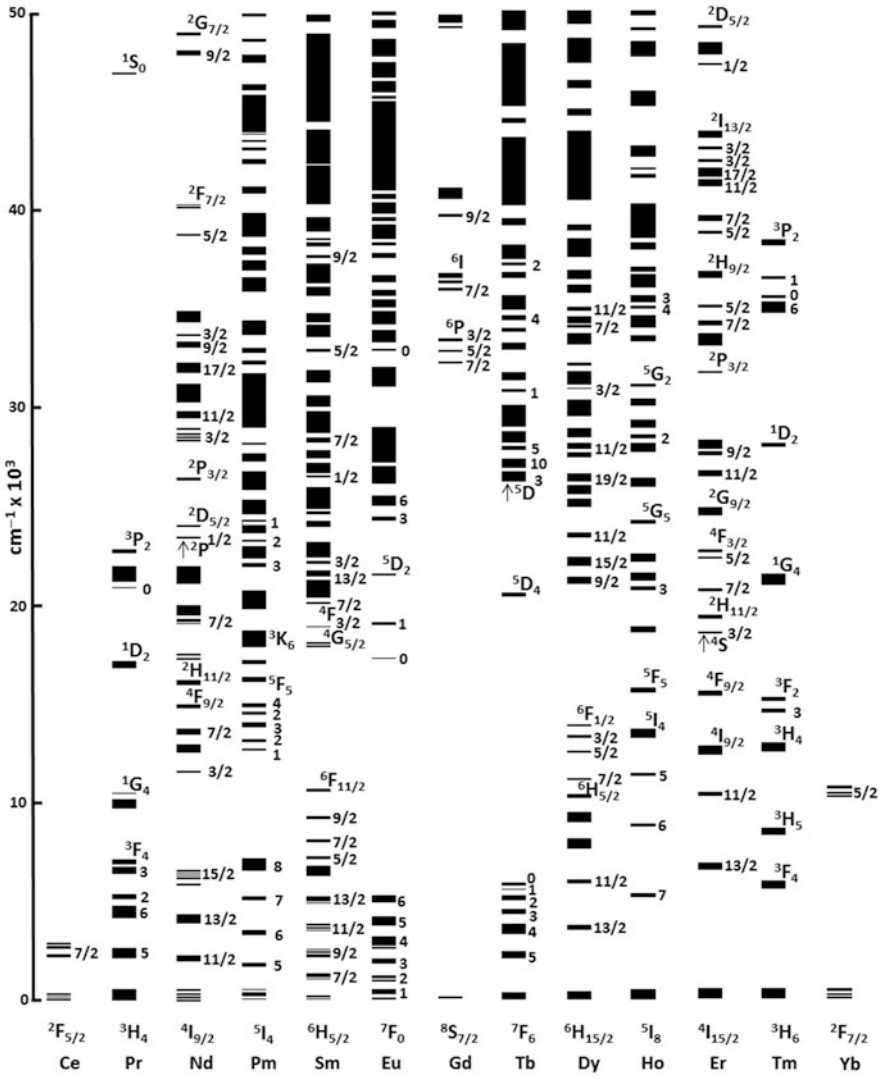

Fig. 4.10 Energy-level structure of Ln^{3+}:LaF_3 based on computed crystal field energies in range 0–50,000 cm^{-1} with labels of ^{2S+1}L and/or J, where the dominant character of the levels can be clearly assigned. This energy-level diagram was reproduced with permission from ref. [28]

the $^7F_0$ ground state, its compounds would be diamagnetic, whereas contributions from thermally accessible levels such as $^7F_1$ and $^7F_2$ [using a Boltzmann factor of exp.$(-\Delta E/kT)$] lead to an observed room-temperature magnetic moment at 3.5 μ_B.

Comparison of the values of the effective magnetic moment (μ_{eff}) calculated from the empirical HUND formula, which is known to fit well with observed magnetic moments for all RE^{3+} except Sm^{3+} and Eu^{3+} ions [129], and by

Table 4.5 Electronic structure and magnetic properties of trivalent rare-earth ions

Z	RE^{3+}	Config. ($4f^n$)	Fund. level	First excited level	ΔE (cm^{-1})	g_J	μ_{calc} spin	μ_{eff} J-Hund	μ_{eff} Van Vleck	μ_{eff} Exp.
57	La	$4f^0$	($^1S_0$)	–	–	–	–	–	–	–
58	Ce	$4f^1$	($^2F_{5/2}$)	($^2F_{7/2}$)	2200	0.86	1.73	2.54	2.56	2.3–2.5
59	Pr	$4f^2$	($^3H_4$)	($^3H_5$)	2100	0.80	2.83	3.58	3.62	3.4–3.6
60	Nd	$4f^3$	($^4I_{9/2}$)	($^4I_{11/2}$)	1900	0.73	3.87	3.62	3.68	3.5–3.6
61	Pm	$4f^4$	($^5I_4$)	($^5I_5$)	1600	0.60	4.90	2.68	2.83	2.7
62	Sm	$4f^5$	($^6H_{5/2}$)	($^6H_{7/2}$)	1000	0.29	5.92	0.84	**1.55–1.65**	**1.5–1.6**
63	Eu	$4f^6$	($^7F_0$)	($^7F_1$)	300	0	6.93	0	**3.40–3.51**	**3.4–3.6**
64	Gd	$4f^7$	($^8S_{7/2}$)	($^6P_{1/2}$)	32,000	2.00	7.94	7.94	7.94	7.8–8.0
65	Tb	$4f^8$	($^7F_6$)	($^7F_5$)	2000	1.50	6.93	9.72	9.7	9.4–9.6
66	Dy	$4f^9$	($^6H_{15/2}$)	($^6H_{13/2}$)	3300	1.33	5.92	10.60	10.6	10.4–0.5
67	Ho	$4f^{10}$	($^5I_8$)	($^5I_7$)	5300	1.25	4.90	10.61	10.6	10.3–0.5
68	Er	$4f^{11}$	($^4I_{15/2}$)	($^4I_{13/2}$)	6500	1.20	3.87	9.58	9.6	9.4–9.6
69	Tm	$4f^{12}$	($^3H_6$)	($^3H_4$)	5800	1.17	2.83	7.56	7.6	7.1–7.4
70	Yb	$4f^{13}$	($^2F_{7/2}$)	($^2F_{5/2}$)	10,000	1.14	1.73	4.54	4.54	4.4–4.9
71	Lu	$4f^{14}$	($^1S_0$)	–	–	–	–	–	–	–

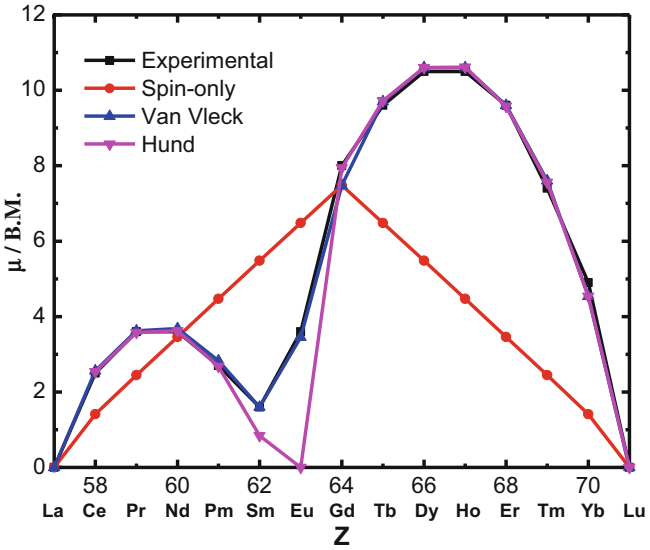

Fig. 4.11 Effective magneton number at room temperature for sequence of trivalent rare-earth ions in configurations $4f^0$, 4f, $4f^2$, ..., $4f^{14}$. Reproduced with permission from ref. [129]

means of the Van Vleck formula [128] gives calculated values that are generally in good agreement with the experimental magnetic moments for all rare-earth ions (Fig. 4.11). The Van Vleck formula describes the dependence of magnetic susceptibility on temperature and is one of the cornerstone relationships in magnetochemistry:

$$\chi(T) = \frac{N\sum_n \left[\frac{\left(E_n^{(1)}\right)^2}{KT} - 2E_n^{(2)} \right] \exp\left(-\frac{E_n^{(0)}}{KT}\right)}{\sum_n \exp\left(-\frac{E_n^{(0)}}{KT}\right)} \tag{4.9}$$

The effective Bohr magneton number (commonly defined as the effective magnetic moment) μ_{eff} is usually deduced from the magnetic susceptibility by the relation

$$\mu_{\text{eff}} = \left(\frac{3K_b \chi^T}{\mu_0 N_A \mu_B^2} \right)^{1/2}. \tag{4.10}$$

The experimental magnetic moments of rare-earth ions in the second half of the series are greater than in the first half (Table 4.5). For RE^{3+} ions, the magnetic moments are attributed to the J ground state values, where $J = L - S$ is lower if the electron number is less than half the $4f^7$ configuration ($n < 7$), and $J = L + S$

is larger if the electron number is greater than 7 in the $4f^n$ configuration ($n > 7$). Thus, the total angular momentum (J) has a key role during the calculation of the magnetic moments in rare-earth ions, and as a result, the spin-only formula cannot be applied to rare-earth ions (Fig. 4.11).

It is noteworthy that the rare-earth elements are good candidates for designing permanent magnets owing to the higher values of their magnetic moments. Therefore, neodymium magnets are the strongest permanent magnets, commercially available, and used in modern technologies such as hard disk drives. This magnet is an alloy of neodymium, iron, and boron, represented by the formula $Nd_2Fe_{14}B$, and has a tetragonal crystalline structure. In addition, among the common magnetic compounds are metal oxides, which are chemically bonded compositions of metals with oxygen, such as iron oxides and ferrites.

4.3.2 Magnetic Induction and Magnetization

When a magnetic field, $\boldsymbol{H}$, is applied to a material, the response of the material is called its *magnetic induction*, $\boldsymbol{B}$. The relationship between $\boldsymbol{B}$ and $\boldsymbol{H}$ is a property of the material and can be expressed by Eq. 4.11 (in centimeter–gram–second, or cgs, units) [127]:

$$\boldsymbol{B} = \boldsymbol{H} + 4\pi\boldsymbol{M}, \tag{4.11}$$

where $\boldsymbol{M}$ is the *magnetization* of the medium and is usually defined as the magnetic moment ($\boldsymbol{m}$) per unit volume ($\boldsymbol{V}$), as shown by Eq. 4.12:

$$\boldsymbol{M} = \frac{\boldsymbol{m}}{\boldsymbol{V}} \frac{\text{emu}}{\text{cm}^3}. \tag{4.12}$$

$\boldsymbol{M}$ is a property of the material and depends on both the individual magnetic moments of the constituent ions, atoms, or molecules and on how these dipole moments interact with each other. The cgs unit of magnetization is the emu/cm^3.

It is sometimes more convenient to express the value of magnetization in unit mass rather than unit volume. The mass of a small sample can be measured more accurately than its volume; moreover, the mass is independent of temperature, whereas the volume changes with temperature owing to thermal expansion. The specific magnetization $\boldsymbol{\sigma}$ is defined as the magnetic moment ($\boldsymbol{m}$) per unit mass ($\boldsymbol{w}$), as given by the expression

$$\boldsymbol{\sigma} = \frac{\boldsymbol{m}}{\boldsymbol{W}} = \frac{\boldsymbol{m}}{\boldsymbol{V}\boldsymbol{\rho}} = \frac{\boldsymbol{m}}{\boldsymbol{\rho}} \frac{\text{emu}}{\text{g}}, \tag{4.13}$$

where $\boldsymbol{V}$ is the volume and $\boldsymbol{\rho}$ the density.

Magnetization can also be expressed as the magnetic moment per mole, per unit cell, per formula unit, and so forth. When dealing with small volumes, such as the

unit cell, the magnetic moment is often given in the Bohr magneton, μ_B, where 1 Bohr magneton $= 9.27 \times 10^{-21}$ erg/Oe.

In SI units the relationship between $\boldsymbol{B}$, $\boldsymbol{H}$, and $\boldsymbol{M}$ is given by the expression [127]

$$\boldsymbol{B} = \boldsymbol{\mu}_0 (\boldsymbol{H} + \boldsymbol{M}), \tag{4.14}$$

where μ_0 is the permeability of free space. The units of $\boldsymbol{M}$ are obviously the same as those of $\boldsymbol{H}$ (A/m), and those of μ_0 are weber/(A m), also known as henry/m. Therefore, the units of $\boldsymbol{B}$ are weber/m^2, or tesla (T); 1 gauss $= 10^{-4}$ T.

Magnetic materials are usually composed of small regions, known as domains, and in each domain the individual magnetic moments of the constituent atoms are aligned with one another and point in the same direction. Magnetic domains are formed in materials that have magnetic ordering, that is, their dipoles spontaneously align owing to the exchange interaction. These materials include ferromagnetic, ferromagnetic, and antiferromagnetic materials. In paramagnetic and diamagnetic materials, the dipoles are aligned in response to an external applied magnetic field and cannot align spontaneously; therefore, they have no magnetic domains. The magnetic domain structure is responsible for the formation of permanent magnets and the attraction of ferromagnetic and ferrimagnetic materials to a magnetic field.

In the case of permanent magnets, the magnetic moments of all or most domains are aligned in a uniform direction to exhibit a net magnetization. In contrast, an unmagnetized magnet possesses domains that are randomly oriented with respect to each other, giving a net magnetization of zero. However, this unmagnetized magnet material can be magnetized if an external high magnetic field $\boldsymbol{H}$ is applied to it; consequently, the domains' magnetic moments are aligned with $\boldsymbol{H}$ to yield a net magnetization $\boldsymbol{M}$ and give an externally observable field whose strength depends on the nature of the magnet material.

4.3.2.1 Magnetization Curves

Irreversible changes in the magnetization of ferrimagnetic and ferromagnetic materials are measured by applying cyclic positive and negative values of the magnetic fields to these materials, yielding curves known as *hysteresis loops*. These measurements initially give a so-called *virgin curve* since the materials come from an unmagnetized or virgin state, which is formed as a result of the magnetization of these materials in the initial stage as the applied field is increased. Then the magnetic structure of the materials is irreversibly altered, preventing this virgin curve from forming, and it is usually withdrawn during experiments.

The magnetization curve of ferrimagnetic and ferromagnetic materials can be illustrated as a graph of $\boldsymbol{B}$ (or $\boldsymbol{M}$) versus $\boldsymbol{H}$, which is also called a *hysteresis loop* (Fig. 4.12). In this case, the magnetic material is started at the origin in an unmagnetized or virgin state, and magnetic induction ($\boldsymbol{B}$) follows the curve from the value of 0 to $\boldsymbol{B}_s$ as the applied magnetic field ($\boldsymbol{H}$) is increased in the positive direction, where $\boldsymbol{B}_s$ is known as *saturation induction* (or $\boldsymbol{M}_s$: *saturation*

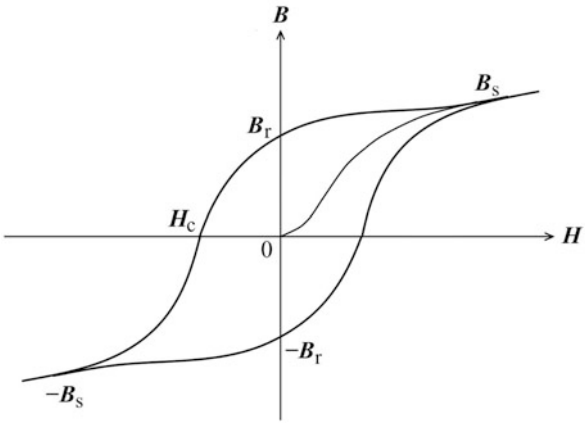

Fig. 4.12 Hysteresis loop for a ferro- or ferrimagnet. Reproduced with permission from ref. [127]

magnetization), which is essentially the limit value to which the curve tends within a high-field region and is reached when all a domain's magnetic moments in a material are aligned with the external field. However, the magnetization ($\boldsymbol{M}$) is constant after saturation, but $\boldsymbol{B}$ continues to increase because $\boldsymbol{B} = \boldsymbol{H} + 4\pi\boldsymbol{M}$ [127]. When $\boldsymbol{H}$ is reduced to zero after saturation, the induction decreases from $\boldsymbol{B}_s$ to $\boldsymbol{B}_r$: *residual induction* (or $\boldsymbol{M}_r$: *remanent magnetisation*), i.e., the material does not recover its unmagnetized state, retaining a certain amount of magnetization at the zero field owing to continued alignment of the domain's magnetic moments in the positive direction. A reversed field in the negative direction that is required to reduce the induction or magnetization to zero is called *coercivity* ($\boldsymbol{H}_C$). Depending on the value of the coercivity, ferromagnetic materials are classified as either hard or soft. Hard magnetic materials require a large field to reduce their induction or magnetization to zero, whereas soft materials are easily saturated but also easily demagnetized. When the reversed field is increased further, saturation is achieved in the reverse or negative direction, which leads to the formation of a hysteresis loop. In the case of superparamagnetic nanoparticles, the magnetization curves show almost zero *remanent magnetization* ($\boldsymbol{M}_r$) and zero *coercivity* ($\boldsymbol{H}_C$) values.

4.4 Luminescence

The term *luminescence* was introduced in 1888 by German physicist Eilhard Wiedemann; it can be explained as the emission of light by certain materials at relatively low temperatures (cold light), to be distinguished from emissions owing to incandescence (hot light), such as fire light, candles, oil lamps, and gas light. Incandescence is usually produced by the direct heating of matter to high temperatures, which results in the emission of light over a continuous range of energies (wavelenghts) in correlation with temperature. Luminescence, by contrast, is the emission of radiation at normal, lower temperatures when luminescent

materials are excited with often invisible energy sources such as ultraviolet light, electric fields, X-rays, energetic particles from radioactive decay, and so on.

Therefore, on the basis of the nature of the exciting source, luminescence is subdivided into a number of categories. Some of the most studied ones are *photoluminescence* (emission after excitation by irradiation with electromagnetic radiation), *electroluminescence* (emission by a recombination of electrons and holes under the influence of an electric field), *radioluminescence* (emission of light upon excitation owing to ionizing radiation), *cathodoluminescence* (emission after excitation with cathode rays), *chemiluminescence* (nonthermal production of light by a chemical reaction), or *triboluminescence* (emission observed by applying mechanical stress to crystals or by the fracture of crystals). Solid materials that give luminescence are called phosphors or, latterly, luminescent materials.

In this chapter, we discuss the luminescence spectroscopy of rare-earth ions (RE^{3+}), and, following the conventions of the International Union of Pure and Applied Chemistry, we usually use *fluorescence* in connection with processes that occur without changes in spin, typically $S_1 \rightarrow S_0$ ($\Delta S = 0$) or Yb^{3+} ($^2F_{5/2} \rightarrow {}^2F_{7/2}$) transitions, and *phosphorescence* for transitions implying a change in spin [130], typically $T_1 \rightarrow S_0$ ($\Delta S \neq 0$) or Eu^{3+} ($^5D_0 \rightarrow {}^7F_J$) transitions.

4.4.1 Rare-Earth Luminescence

Rare-earth elements include lanthanides, ranging from lanthanum to lutetium (Ln: La, Ce, Pr, Nd, Pm, Sm, Eu, Gd, Tb, Dy, Ho, Er, Tm Yb, Lu), scandium (Sc), and yttrium (Y). These elements have similar physical and chemical properties. The similarity of trivalent lanthanide ions to each other, especially to their neighbors, are due to their general adaptation of the +3 oxidation state in aqueous solution, which causes their separation to be an extremely difficult process. The rare earths usually occur in compounds as RE^{3+} ions; other oxidation states are stable only when an empty ($4f^0$), half-filled ($4f^7$), or full ($4f^{14}$) subshell is produced. The predominant oxidation state is trivalent (Ln^{3+}, Sc^{3+}, Y^{3+}), though divalent (Sm^{2+}, Eu^{2+}, Tm^{2+}, Yb^{2+}) and tetravalent states (Ce^{IV}, Pr^{IV}, Tb^{IV}) can also be encountered. The electronic configuration of RE^{3+} ions is represented by $[Xe]4f^n$, which shows a gradual increase in the number of electrons n with increasing the atomic numbers of the ions [31], ranging from $4f^0$ to $4f^{14}$ for La^{3+} to Lu^{3+} ions.

RE^{3+} ions exhibit a number of features in their chemistry that differentiate them from the d-block metals: (1) high coordination numbers (generally between 6 and 12); (2) coordination geometries that are determined by ligand steric factors rather than ligand field effects; (3) formation of labile "ionic" complexes that undergo facile exchanges of ligands; (4) small ligand field splitting and very narrow emission and absorption bands in comparison with d-block metals; (5) a preference for anionic ligands with donor atoms even of high electronegativity (e.g., N, O, F); (6) ready formation of hydrated complexes (on account of the high hydration energy of the small Ln^{3+} ion).

The remarkable feature of RE^{3+} ions is their photoluminescence behavior; some of them show luminescence in the visible or NIR spectral regions under a UV irradiation lamp. The color of the emitted light depends on the RE^{3+} ion. For instance, Eu^{3+} emits in red, Tb^{3+} in green, Sm^{3+} in orange, and Tm^{3+} in blue light. Yb^{3+}, Nd^{3+}, and Er^{3+} ions are well known for their NIR luminescence [25]. In addition, Pr^{3+}, Sm^{3+}, Dy^{3+}, Ho^{3+}, and Tm^{3+} ions also show transitions in the NIR region, and Gd^{3+} emits in the UV region.

4.4.1.1 Luminescence Spectroscopy of Rare-Earth Ions

The optical properties of rare-earth ions are fascinating and originate in the special features of the electronic $[Xe]4f^n$ configurations ($n = 0$–14). The more common oxidation states are +3, +2, and +4. However, the +3 oxidation state is characteristic of all rare-earth ions that show a $4f^n$ configuration. These 4f configurations generate a rich variety of electronic levels whose number is given by $[(4l + 2)!/(4l + 2 - n)n!]$, yielding 3003 sublevels for Eu^{3+} and Tb^{3+} ions. They are characterized by three quantum numbers, S, L, and J within the frame of a Russell–Saunders spin–orbit coupling scheme [32]. The energies of these levels are well defined owing to the shielding of 4f electrons by the filled $5s^25p^6$ subshells, and they are not very sensitive to the chemical environments in which the rare-earth ions are placed. Therefore, in RE^{3+} complexes the ligands in the first and second coordination spheres perturb and split the $^{2S+1}L_J$ energy levels of the RE^{3+} ions only slightly. This shielding is responsible for the specific properties of the rare-earth luminescence, more particularly the narrow emission bands and the long lifetimes of the excited states owing to forbidden 4f–4f transitions. Moreover, in particular, Ce^{3+} ions show intense broad emission bands due to the allowed f–d transitions, and the position of the emission maximum strongly depends on the ligand environment of the Ce^{3+} ions [131]. The 4f–4f transitions are parity forbidden; however, Laporte's rule is slightly relaxed for these transitions owing to the mixing of opposite parity electronic configurations produced by the odd components of a noncentrosymmetric ligand field. Moreover, ligand polarization effects have been shown to be of considerable importance for 4f–4f transitions.

The existence of different energy levels (Fig. 4.10) for rare-earth ions is a consequence of different interactions operating in the $4f^n$ electronic configuration of ions. Depending on the number, the electrons can distribute in many ways over the $4f^n$ configurations; however, some distributions are energetically more favorable. Each different electronic arrangement is called a *microstate*. For systems with more than one $4f^n$ electron, such as Eu^{3+} ions ($4f^6$) [132], the degeneracy of the $4f^n$ configuration is partly or totally lifted by several perturbations acting on the RE^{3+} ions: electron repulsion, spin–orbit coupling, ligand field perturbation, and eventually the Zeeman effect (Fig. 4.13). Electron repulsion is the electrostatic interaction between different electrons in a 4f subshell. Spin–orbit coupling results from interactions between the spin magnetic moment and the orbital magnetic moment of electrons. The ligand field effect is caused by interactions between 4f

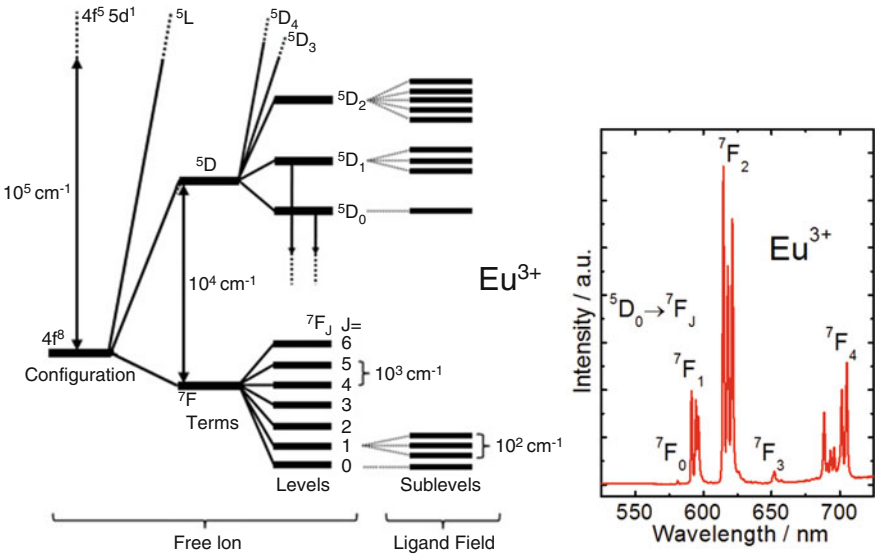

Fig. 4.13 Partial energy diagram of Eu^{3+} ($4f^6$) (*left*) showing relative magnitude of interelectronic repulsion (terms), spin–orbit coupling (levels), and crystal-field effects (sublevels). The *downward arrows* indicate the excited states $^5D_0$ and $^5D_1$ from which luminescence occurs. Reproduced with permission from ref. [132]. Emission spectrum (*right*) of Eu^{3+} complex

electrons and electrons of the ligands. The Zeeman effect is the splitting of energy levels by an external magnetic field.

Electrostatic repulsion splits the electronic configuration into spectroscopy terms labeled by "^{2S+1}L" according to the spin multiplicity $2S + 1$ and the total angular momentum L with a separation at around 10^4 cm^{-1} (Fig. 4.13). The terms are usually denoted by capital letters of the Latin alphabet, for example, S ($L = 0$), P ($L = 1$), D ($L = 2$), F ($L = 3$), G ($L = 4$), H ($L = 5$), I ($L = 6$), K ($L = 7$), L ($L = 8$), M ($L = 9$). Notice that the letter J is not used as a term label. The nomenclature for spin multiplicity is singlet, doublet, triplet, quartet, quintet, sextet, and septet for $2S + 1 = 1, 2, 3, 4, 5, 6, 7$, respectively [132]. The spin–orbit interaction (between two magnetic dipoles) removes the degeneracy of the ^{2S+1}L spectroscopy terms into J levels of free ions characterized by L, S, J quantum numbers and labeled by $^{2S+1}L_J$ levels. These levels are relatively higher (10^3 cm^{-1}) because of the heavy rare-earth nucleus (Fig. 4.13). The energy levels of a *free ion* can be described by $^{2S+1}L_J$ levels, where $2S + 1$ represents the total spin multiplicity, L the total orbital angular momentum, and J the total angular momentum of 4f electrons.

On placing RE^{3+} ions in a chemical environment, such as organic ligands or inorganic matrices, the spherical symmetry of free ions is destroyed and each spectroscopic level (J-levels) further splits under the influence of the asymmetric electric field produced by the chemical environment, called a ligand field or crystal field. This interaction removes, to a certain degree, the degeneracy of free-ion levels.

The magnitude of the splitting of the $^{2S+1}L_J$ energy levels was first parameterized in the simplest way assuming a point charge electrostatic model (PCEM) generated by the chemical environment around the rare-earth ions. The ligand field effect (H_{LF}) further lifts the $(2J + 1)$ degeneracy of the J levels in free ions, depending exclusively on the point of symmetry about the RE^{3+} ions [31], which are called crystal-field levels (or Stark levels). The splitting of the energy levels by the ligand field effect is of the order of a few hundred per centimeter (around 10^2 cm^{-1}).

Luminescence originating from intraconfigurational d transitions is quite different from that of 4f–4f ones. The spectra of d metals are much poorer in the number of observed pure zero-phonon transitions since d^n configurations have much fewer microstates than $4f^n$ ones. The vibronic interaction is much stronger than those of 4f–4f transitions. In addition, for d-transition elements, the ligand field interaction is at least one order of magnitude greater due to the nonscreened and more extended d radial distribution. These facts produce very broad d–d transition bands [29]. Transition-metal complexes usually have lower coordination numbers (4 and 6) than f elements. In the case of fourfold tetrahedral coordination, d–p mixing relaxes Laporte's rule, allowing for d–d transitions, while in the case of octahedral coordination Laporte's rule is not relaxed, except for vibronic interactions that instantaneously break down the center of inversion and allow for the d–d transitions, with much weaker intensities than in the tetrahedral case. Ligand polarization effects on d–d transitions, to our knowledge, have not yet been investigated.

4.5 Biomedical Applications

4.5.1 Bioimaging

Multimodal imaging may play an important role in the diagnoses of diseases and perhaps replace conventional single imaging techniques in the near future, such as magnetic resonance imaging (MRI), X-ray computed tomography (CT), positron emission tomography (PET), single-photon emission computed tomography (SPECT), and fluorescent imaging (FI) [133]. Bifunctional optical and magnetic nanomaterials can be used as agents to combine both magnetic resonance and fluorescent imaging, in order to record multiple images of the anatomical and physiological processes of the body at the same time with enhanced resolution and quality. In this case, the magnetic property of bifunctional nanomaterials can be used as a contrast agent for MRI and the photonic behavior as a tool for fluorescent imaging. However, to the best of our knowledge, little research has been dedicated to multimodal imaging, and MRI is still popular in medical diagnosis.

Magnetic resonance imaging, also known as magnetic resonance tomography (MRT), is a noninvasive medical imaging technique used in diagnosis to capture detailed three-dimensional images of the anatomy of various organs of the body in both health and disease without the use of deleterious radiation. MRI operates on the basis of applying a strong magnetic field and radio frequency waves, so

proton nuclei are decayed by transverse magnetization (T_2 relaxation) in order to recover the longitudinal magnetization (T_1 relaxation), which produce electrical radio signals. The durations of T_1 and T_2 relaxations vary in different tissues depending on their composition and nature. However, the relaxation times of various tissues, tumors, and physiological process are superimposed on each other, which makes the dynamic scan and resolution of images difficult to measure. Therefore, to enhance the clarity of imaging, various contrast agents are used to increase or decrease the T_1 and T_2 relaxation times. Functionally, MRI contrast agents can be divided into two groups: T_1 and T_2 contrast agents. Among the T_1 contrast agents, generally Gd^{3+} chelates and, to a lesser extent, Mn^{2+} chelates are widely used; however, gadolinium in the free ionic state is toxic and causes several clinical diseases [134], such as severe allergic reactions, nephrogenic system fibrosis, and kidney failures.

Bifunctional optical and magnetic nanomaterials have been studied for application in MRI, for instance, $Fe_3O_4@SiO_2@GdVO_4:Eu^{3+}$ (5 mol%) nanomaterial shows intense red luminescence and strong magnetism with no cytotoxicity against human erythrocytes and has been proposed as a good candidate for MRI [135]. Recently, Chen and coworkers [136] have reported on bifunctional Poly(MMA-HEMA $Eu(AA)_3Phen)/Fe_3O_4$ nanospheres as a good T_2-weighted MRI contrast agent and for optical imaging with good biocompatibility and 85% cell viability, even at concentrations has high as 1240 $\mu g\ mL^{-1}$. In addition, multifunctional magnetic/upconversion luminescent $Fe_3O_4@LaF_3:Yb^{3+},Er^{3+}$ mesoparticles show efficient T_2 enhancement in MRI with a T_2 relaxivity coefficient (r^2) value of 229 $mM^{-1}S^{-1}$ [86]. In vivo study of multifunctional $NaYF_4:Yb^{3+},Tm^{3+}@Fe_xO_y$ with histological analysis and MTT assays suggest these materials show low toxicity, good biocompatibility, and enhanced T_2 MRI [137]. Moreover, multifunctional $Fe_3O_4@NaLuF_4:Yb^{3+},Er^{3+}/Tm^{3+}$ nanostructures have exhibited good T_2-enhanced MRI with an r^2 value of 21.63 $s^{-1}\ mM^{-1}$ at 0.5 T and low cytotoxicity [138].

In different experiments, owing to the large magnetic moment of superparamagnetic Fe_3O_4, various multifunctional nanomaterials, such as $Fe_3O_4@Y_2O_3:Eu^{3+}$ /PMMA [139], Fe_3O_4-decorated $YPO_4:Eu^{3+}$ hybrid nanostructures by covalent bridging of carboxyl PEGylated Fe_3O_4 and amine-functionalized $YPO_4:Eu^{3+}$ particles [106], $Fe_3O_4@LaF_3:Ce^{3+},Tb^{3+}$ composite nanoparticles [140], $Fe_3O_4@SiO_2@GdVO_4:Dy^{3+}$ [141], $NaYF_4:Yb^{3+},Er^{3+}@Fe_3O_4@Au$ [142], and $Fe_3O_4/SiO_2/NH_2/PAA/CeF_3:Gd^{3+}$ (10%),Tb^{3+} (10%) [143], have been proposed as promising candidates for magnetic resonance contrast agents.

4.5.2 Hyperthermia

Hyperthermia, also known as thermotherapy, compared to conventional radiotherapy is the most potent medical treatment of cancer by magnetically generated heat from MNPs administered at a desired site such as a tumor. It is also known as

thermoradiotherapy when it is combined with radiation therapy [144]. In hyperthermia, when the desired site containing MNPs is exposed to an alternating current magnetic field (ACMF) within a proposed safe frequency range of approximately 100–400 kHz, nanoparticles begin to emit heat via Néel and Brownian pathways [145, 146], increasing the temperature of the surrounding tissue, which either kills the cells or makes them more susceptible to further radiation or drug treatment.

Ideally the viability of cancerous cells can be reduced to a large extent in a temperature range of 42–46 °C. On the basis of the generated temperature variability, there are two types of hyperthermia therapy: (1) thermal ablation at a temperature of >50 °C for a short time period of 10–30 min and (2) mild hyperthermia at a temperature of 42–45 °C for 30 min [147]. Hyperthermia therapy also acts by damaging the blood vasculature, impairing nutrient and oxygen supplies, or dilating blood vessels, where increased blood flow can carry large amounts of drug and oxygen, which is a potent radio sensitizer that makes tumor cells more susceptible to radiotherapy. It also causes a deterioration of tumor cells by the entropy of cellular structures [148, 149], such as DNA and protein, and immunological cells kill them as well, leading to tissue necrosis.

Note that the specific absorption rate (SAR) and the particle size are more important for achieving an adequate temperature in hyperthermia treatment. Therefore, MNPs are designed in such a way as to give a reasonably small size and maximum SAR [150]. The power released by the MNPs is assessed by their SAR or their specific losses per cycle (SLPC) denoted by A, linked by the equation $\mathrm{SAR} = Af_{\mathrm{exc}}$, where A is the area of the hysteresis loop and f the sweeping frequency of the magnetic field. An increase in SAR above 1 kW g^{-1} could be beneficial regarding several aspects of hyperthermia applications, but it represents a significant challenge.

Recently, significant research interest has been dedicated to designing bifunctional nanomaterials with efficient luminescent and magnetic properties for cancer therapy with hyperthermia. The luminescence properties of these nanomaterials can act as an internal thermometer to monitor changes in temperature of the surrounding tissues due to the heat generated by these magnetic particles deposited in corresponding tissues under the influence of an AC magnetic field. Therefore, several attempts have been made to develop multifunctional nanocomposites showing high thermal energy transfer capability, combining efficient magnetic and optical material in a single biocompatible nanostructure entity.

Among these nanomaterials, $YPO_4:Tb^{3+}@Fe_3O_4$ has been studied for magnetic hyperthermia, which produces a temperature of 42 °C with an SAR value of 39.22 W g^{-1} under an AC magnetic field of 110 Oe and 425 kHz frequency in 10 min [151]. Fe_3O_4–$CaMoO_4:Eu^{3+}$ hybrid MNPs present a good heating capacity, achieving 42 °C temperature in 9 min under the 300 A applied current and within 4.3 min, using 400 A applied current with 19 W g^{-1} and 26 W g^{-1} SARs values, respectively [107]. In addition, SnO_2:5Tb/Fe_3O_4 nanoparticles generate 42 °C at 300 and 400 A in 149 and 57 s with SAR values of 37 and 53 W g^{-1}, respectively [152]. Hybrid nanomaterials of $CaF_2:Eu^{3+}$, Mn^{2+}, and Fe_3O_4 have demonstrated the an ability to produce a temperature of 42 °C under an AC magnetic field

of 265 kHz and 335 Oe with a very high SAR of 283 W g^{-1} [9], while with Fe_3O_4@YPO_4:Eu^{3+} a hyperthermia temperature of 42 °C was obtained at a 400 A current within 10 min [153]. Therefore, these previously reported results suggest that optical and magnetic nanomaterials may be strong candidates for magnetic hyperthermia with self-monitoring temperature capability but will still represent a challenge in the field of medical therapies for cancer.

4.5.3 Drug Delivery

Drug delivery is engineered technology for the controlled administration of pharmaceutical compounds to a tissue of interest in order to achieve the maximum concentration of therapeutic agents while reducing the concentration in other tissues. Initial attempts to manipulate devices in the body with extracorporeal magnets began in the 1950s. Thus, owing to recent advancements in nanotechnology, interest in magnetic drug targeting has grown significantly [154], including the use of iron oxides—magnetite (Fe_3O_4) and maghemite (γ-Fe_2O_3) nanoparticles—as drug delivery vehicles for therapeutic applications exploiting magnetic systems.

Drug carrier MNPs are usually based on a core of iron oxide coated with silica, gold, or polymer, for example, to functionalize and load easily with the corresponding drug molecules. Maghemite (γ-Fe_2O_3) is one of the most suitable materials for the core of MNPs because it is causes fewer health hazards, and Fe^{3+} ions are widely found in the human body. On the other hand, the use of magnetite (Fe_3O_4) nanoparticles can be detrimental owing to the release of Fe^{2+} ions, which generate toxic hydroxyl radicals via Fenton reactions [155]. Drug molecules are loaded in various ways to magnetic iron oxide–based drug delivery vehicles: they are (1) linked directly to the activated surfaces of iron oxide nanoparticles, (2) encapsulated together in stimulus-responsive hydrogel/polymer frameworks, (3) trapped in magnetoliposomes, and (4) loaded in the polymer interspace of magnetic nanoclusters [156]. These cargo particles are guided by an external magnetic field to the target tissues, where they are unloaded by different mechanisms, such as varying the pH, osmolality, temperature generated by an external alternating magnetic field (e.g., for superparamagnetic iron oxide nanoparticles), heating with shortwave radio-frequency fields, irradiation with ultraviolet, visible light or NIR light, and by enzymatic activity.

Recently, multifunctional nanomaterials coassembling luminescent and magnetic features into single nanoparticles are the subject of great research interest owing to their therapeutic application as targeted drug delivery vehicles. In this case, the superparamagnetic and luminescent properties of these nanoparticles allow for the visualization of targeted locations (e.g., tumors) using T_2-wieghted MRI and fluorescent imaging [157], whereas magnetic behavior can also be utilized to manipulate and deliver a drug to a target with extracorporeal magnets, providing a new tool for understanding the physiochemical process of cells in developing cancer tissues.

Multifunctional magnetic iron oxide nanoparticles functionalized with inorganic materials, lipids, or polymers not only act as carriers of targeted drugs but also have potential in therapeutic and diagnostic applications. For instance, multifunctional (SPION–DOX–PEG–FA) nanoparticles have been studied as bimodal cancer cell imaging agents [158] and in bimodal cancer treatment through hyperthermia effects and targeted drug delivery. Iron oxide nanoparticles not only act as drug carriers but also as vehicles for targeted gene delivery. Qiu and coworkers [159] reported on stearic-LWPEI-SPIO nanoparticles, which showed a high binding capacity for minicircle DNA (mcDNA), protection efficiency from enzymatic degradation, and a controlled release property in the presence of polyanionic heparin. In addition, stearic-LWPEI-SPIO nanoparticles have been employed successfully in MRI visible delivery of mcDNA.

Upconversion luminescent nanoparticles (UCNPs) have emerged as promising candidates for traceable drug delivery because of their upconversion luminescence and biocompatible properties. On the basis of a drug loading procedure, UCNPs can be classified into three categories: (1) hydrophobic drugs (e.g., doxorubicin), which are encapsulated into hydrophobic pockets generated by polyethylene glycol (PEG)–grafted amphiphilic polymers that are bounded to ligands (e.g., oleic acid) via van der Waals interactions on the surfaces of $NaYF_4$:Yb^{3+},Er^{3+} UCNPs. The release of drug is then controlled by varying the pH in acidic tumor cells [160]; (2) drugs (e.g., ibuprofen) that are deposited in the pores of mesoporous silica shells coated onto the surface of β-$NaYF_4$:Yb^{3+},Er^{3+} UCNPs fibers [161]; (3) drugs that are commonly loaded in hollow spheres created by mesoporous UCNP shells made of rare earth ion–doped $NaYF_4$ materials [162] containing inner MNPs.

Carbon nanotubes (CNTs) decorated with MNPs have also gained attention as promising nanocarriers for targeted drug delivery thanks to their distinct characteristics such as enhanced cellular specificity and uptake, high surface area, and easy conjugation with great therapeutic value and diminished side effects. For instance, Singh and coworkers [163] have reported on the use of magnetic CNTs unsheathed with mesoporous silica to facilitate the loading of bioactive molecules. Mesoporous and magnetic hybrid CNTs exhibited excellent magnetic properties and a high loading capacity for therapeutic molecules, including the drug gentamicin and the protein cytochrome C. In addition, genetic molecules, such as small interfering RNA (siRNA), have also loaded effectively and then released over a period of several days to a week. Consequently, multifunctional magnetic nanomaterials are efficient candidates not only for targeted delivery of drugs but also for targeted delivery of genetic molecules.

4.5.4 Biosensors

Biosensors are composite analytical devices consisting of highly sensitive biological or biologically derived recognition components that interact with target analytes and physiochemical components (transducers) that generate signals. They are used to

detect and monitor various biochemical and physiological life processes [164]. The working principle of these devices involves the binding of desired target species to biorecognition elements fixed on a suitable support matrix connected to a transducer. The binding of analytes causes changes in the physical or chemical properties of bioreceptive elements together with the support matrix, which can then be sensed by a transducer to generate an electrical signal. This generated signal quantifies the amount of analyte deposited on the system.

Nanotechnology-based nanobiosensors utilizing nanocantilevers as transducers can provide extreme sensitivity in the detection of targeted species such as biomolecules down to the level of a single particle [164, 165]. Biosensing strategies based on MNPs offer great advantages over other sensing techniques. For instance, MNPs are inexpensive to prepare, physically and chemically stable, biocompatible, and environmentally safe. In addition, biological samples usually exhibit no magnetic background; therefore, highly sensitive measurements can be performed in turbid or otherwise visually obscured samples without further processing [166]. MNP-based sensing has remarkable applications in tissue matching, gene analysis, detection of genetic disorders, forensic applications, and for taking immediate action against infectious agents or onsite emergent contaminations. These biosensors are virtually designed via the immobilization of biological recognition elements of DNA, for example, enzymes, tissue, antibodies, microorganisms, cell receptors, and organelles on the surface of magnetic nanoparticles. In addition, to date, numerous methods have been developed to sense biomolecules using magnetic labels. These methods include various techniques that use magnetometers, such as SQUID, magnetoresistive sensors, and Hall sensors to directly detect magnetic particles.

CNTs are also among the most studied materials in sensing and biosensing applications since they have a large surface area, controlled nanostructure, chemical and thermal stability, and good electronic and optical features. Recently, Fe_3O_4@SiO_2-decorated multiwalled carbon nanotube (MWCNT) nanocomposites have been employed to fabricate a modified carbon-paste electrode (CPE) for the sensing of uric acid [167]. In addition, multifunctional nanostructures based on Fe_3O_4 nanoparticles and carbon nanomaterials, such as graphene oxide (GO) and reduced graphene oxide (rGO), have been used for a variety of applications. Teymourian and coworkers [168] reported on Fe_3O_4-decorated rGO nanosheets for the electrochemical sensing of various analytes, such as ascorbic acid, uric acid, dopamine, NADH, and nitric acid.

Rare-earth materials are promising candidates for biodetection and bioimaging, owing to their low toxicity, high photothermal stability, notable electronic structures, long luminescence lifetimes, and tunable emission colors from UV (Gd^{3+}) to visible (Sm^{3+}, Eu^{3+}, Tb^{3+}, Dy^{3+}) and NIR (Nd^{3+}, Yb^{3+}, Er^{3+}) regions [32, 169]. Moreover, they have the capability for time-resolved fluorescence imaging in the quantitative detection of genes, tissue-specific transcripts, and antigens and can be used effectively for the noninvasive, nondestructive, and real-time in vivo diagnosis of various diseases. Nichkova and coworkers [170] reported on the application of poly(L-lysine)-encapsulated Gd_2O_3:Eu^{3+} nanoparticles as fluorescent labels in competitive fluorescence microarray immunoassays to detect phenoxybenzoic acid.

$YVO_4:Eu^{3+}$ nanoparticles have also been used as luminescent probes for the detection of rabbit immunoglobulin G (IgG) analyte [171] through a sandwich immunoassay strategy.

Upconversion luminescent materials are generally more advantageous for biosensing because they produce no autofluorescence from cells and tissues and are excited by nondeleterious NIR light that has strong penetration ability and high detection sensitivity [172]. Niedbala and coworkers [173] have reported the application of upconversion phosphors to detect amphetamine, the opiate methamphetamine, and phencyclidine in saliva, utilizing a lateral flow–based strip assay. In addition, MnO_2-modified $NaYF_4:Yb^{3+},Tm^{3+}@NaYF_4$ upconversion nanoparticles have also been used for the selective and abrupt sensing of glutathione in living cells [174]. On the basis of these reported results, it can be suggested that in the future, highly sensitive biosensor devices will be designed by combining highly target-specific biological sensing elements, such as antibodies and magnetic luminescent nanomaterials, in a nanoprobe. This system will be operational on the basis of principles involving changes in either the optical or magnetic properties of nanoprobes as target materials are attached to biorecognition elements. These changes will be measurable by optical or magnetic sensors fixed in the devices, which remains a challenge in nanobiotechnology and medical diagnosis.

4.6 Conclusions

The reduction in the size of materials to the nanoscale level leads to profound changes in internal structures, which in turn greatly modifies the electronic, optical, and magnetic properties of the materials in comparison with their bulk counterparts. Thus, various research groups in science and engineering disciplines are focusing on nanoscale materials. In addition, hundreds of peer-reviewed articles have been published in various scientific journals on bifunctional nanomaterials that coassemble magnetic and photonic features into single-entity nanostructures, examining their magnetic and luminescent properties as well as their applications in various fields, from biomedical diagnosis and therapy to materials science. These bifunctional nanomaterials are usually based on MNPs and trivalent rare-earth ions or iron oxide nanoparticles functionalized with QDs, fluorescent dyes, and luminescent complexes. In this chapter, we provided a concise presentation of various strategies adopted in the design of bifunctional nanomaterials, including synthesis methods of magnetic core nanoparticles, magnetism and luminescence behaviors, and multimodal biomedical applications of bifunctional nanomaterials. To the best of our knowledge, this is the first time detailed information on bifunctional luminescent and magnetic nanomaterials has been summarized in chapter form. We hope the chapter will prove beneficial to both nonspecialists and those working on optical and magnetic nanomaterials.

Acknowledgments The authors are grateful for the financial support of the Coordenação de Aperfeiçoamento de Pessoal de Nível Superior (CAPES, Brazil), Conselho Nacional de Desenvolvimento Científico e Tecnológico (CNPq, Brazil), the World Academy of Sciences (TWAS) for the advancement of science in developing countries, and Fundação de Amparo à Pesquisa do Estado de São Paulo (FAPESP, Brazil). Priscila V. Khan is gratefully acknowledged for her assistance in the preparation of the figures.

References

1. Khan LU, Brito HF, Hölsä J, Pirota KR, Muraca D, Felinto MCFC, Teotonio EES, Malta OL (2014) Red-green emitting and superparamagnetic nanomarkers containing Fe_3O_4 functionalized with calixarene and rare earth complexes. Inorg Chem 53:12902–12910
2. Li X, Zhao D, Zhang F (2013) Multifunctional upconversion-magnetic hybrid nanostructured materials: synthesis and bioapplications. Theranostics 3:292–305; Khan LU, Muraca D, Brito HF, Pirota KR, Felinto MCFC, Teotonio EES, Malta OL (2016) Optical and magnetic nanocomposites containing $Fe_3O_4@SiO_2$ grafted with Eu^{3+} and Tb^{3+} complexes. J Alloys Compd 686:453–466
3. Zhang F, Braun GB, Pallaoro A, Zhang Y, Shi Y, Cui D, Moskovits M, Zhao D, Stucky GD (2012) Mesoporous multifunctional upconversion luminescent and magnetic "nanorattle" materials for targeted chemotherapy. Nano Lett 12:61–67
4. Cheng L, Yang K, Li Y, Chen J, Wang C, Shao M, Lee S-T, Liu Z (2011) Facile preparation of multifunctional upconversion nanoprobes for multimodal imaging and dual-targeted photothermal therapy. Angew Chemie Int Ed 50:7385–7390
5. Cheng L, Yang K, Li Y, Zeng X, Shao M, Lee S-T, Liu Z (2012) Multifunctional nanoparticles for upconversion luminescence/MR multimodal imaging and magnetically targeted photothermal therapy. Biomaterials 33:2215–2222
6. Son A, Dhirapong A, Dosev DK, Kennedy IM, Weiss RH, Hristova KR (2008) Rapid and quantitative DNA analysis of genetic mutations for polycystic kidney disease (PKD) using magnetic/luminescent nanoparticles. Anal Bioanal Chem 390:1829–1835
7. Espinosa A, Di Corato R, Kolosnjaj-Tabi J, Flaud P, Pellegrino T, Wilhelm C (2016) Duality of iron oxide nanoparticles in cancer therapy: amplification of heating efficiency by magnetic hyperthermia and photothermal bimodal treatment. ACS Nano 10:2436–2446
8. Shi D, Sadat ME, Dunn AW, Mast DB (2015) Photo-fluorescent and magnetic properties of iron oxide nanoparticles for biomedical applications. Nanoscale 7:8209–8232
9. Singh LP, Srivastava SK, Mishra R, Ningthoujam RS (2014) Multifunctional hybrid nanomaterials from water dispersible $CaF_2:Eu^{3+},Mn^{2+}$ and Fe_3O_4 for luminescence and hyperthermia application. J Phys Chem C 118:18087–18096
10. Gai S, Yang P, Li C, Wang W, Dai Y, Niu N, Lin J (2010) Synthesis of magnetic, up-conversion luminescent, and mesoporous core-shell-structured nanocomposites as drug carriers. Adv Funct Mater 20:1166–1172
11. Kim H, Achermann M, Balet LP, Hollingsworth JA, Klimov VI (2005) Synthesis and characterization of Co/CdSe core/shell nanocomposites: bifunctional magnetic-optical nanocrystals. J Am Chem Soc 127:544–546
12. Kaewsaneha C, Tangboriboonrat P, Polpanich D, Elaissari A (2015) Multifunctional fluorescent-magnetic polymeric colloidal particles: preparations and bioanalytical applications. ACS Appl Mater Interfaces 7:23373–23386
13. Lin Y-S, Wu S, Hung Y, Chou Y, Chang C, Lin M, Tsai C, Mou C-Y (2006) Multifunctional composite nanoparticles: magnetic, luminescent, and mesoporous. Chem Mater 18:5170–5172

14. Zhang L, Liu B, Dong S (2007) Bifunctional nanostructure of magnetic core luminescent shell and its application as solid-state electrochemiluminescence sensor material. J Phys Chem B 111:10448–10452
15. Laurent S, Forge D, Port M, Roch A, Robic C, Vander Elst L, Muller RN (2008) Magnetic iron oxide nanoparticles: synthesis, stabilization, vectorization, physicochemical characterizations, and biological applications. Chem Rev 108:2064–2110
16. Sharma R, Bansal S, Singhal S (2015) Tailoring the photo-Fenton activity of spinel ferrites (MFe_2O_4) by incorporating different cations (M = Cu, Zn, Ni and Co) in the structure. RSC Adv 5:6006–6018
17. Sun S, Zeng H, Robinson DB, Raoux S, Rice PM, Wang SX, Li G (2004) Monodisperse MFe_2O_4 (M = Fe, Co, Mn) nanoparticles. J Am Chem Soc 126:273–279
18. Zhang Y, Shi Q, Schliesser J, Woodfield BF, Nan Z (2014) Magnetic and thermodynamic properties of nanosized Zn ferrite with normal spinal structure synthesized using a facile method. Inorg Chem 53:10463–10470
19. Blanco-Gutiérrez V, Gallastegui JA, Bonville P, Torralvo-Fernández MJ, Sáez-Puche R (2012) MFe_2O_4 (M: Co^{2+}, Ni^{2+}) nanoparticles: mössbauer and X-ray absorption spectroscopies studies and high-temperature superparamagnetic behavior. J Phys Chem C 116:24331–24339
20. Jacintho GVM, Brolo AG, Corio P, Suarez PZ, Rubim JC (2009) Structural investigation of MFe_2O_4 (M = Fe, Co) magnetic fluids. J Phys Chem C 113:7684–7691
21. Kim KJ, Lee HS, Lee MH, Lee SH (2002) Comparative magneto-optical investigation of d–d charge–transfer transitions in Fe_3O_4, $CoFe_2O_4$, and $NiFe_2O_4$. J Appl Phys 91:9974
22. Fontijin WFJ, van der Zang PJ, Devillers MAC, Metselaar R (1997) Optical and magneto-optical Kerr spectra of Fe_3O_4 and Mg^{2+}-or Al^{3+}-substituted Fe_3O_4. Phys Rev B 56:5432–5442
23. Tilley RJD (2010) Colour and the optical properties of materials. Wiley, Chichester
24. Yu C-J, Wu S-M, Tseng W-L (2013) Magnetite nanoparticle-induced fluorescence quenching of adenosine triphosphate–BODIPY conjugates: application to adenosine triphosphate and pyrophosphate sensing. Anal Chem 85:8559–8565
25. Binnemans K (2009) Lanthanide-based luminescent hybrid materials. Chem Rev 109:4283–4374
26. Borges AS, Dutra JDL, Freire RO, Moura RT, Da Silva JG, Malta OL, Araujo MH, Brito HF (2012) Synthesis and characterization of the europium(III) pentakis(picrate) complexes with imidazolium counter cations: structural and photoluminescence study. Inorg Chem 51:12867–12878
27. Bünzli J-CG, Eliseeva SV (2013) Intriguing aspects of lanthanide luminescence. Chem Sci 4:1939–1949
28. Carnall WT, Goodman GL, Rajnak K, Rana RS (1989) A systematic analysis of the spectra of the lanthanides doped into single crystal LaF_3. J Chem Phys 90:3443–3457
29. Brito HF, Malta OL, Felinto MCFC, Teotonio EES (2009) Luminescence phenomena involving metal enolates. In: Zabicky J (ed) The chemistry of metal enolates—part 1. Wiley, Chichester, pp 131–184
30. de Sá GF, Malta OL, de Mello DC et al (2000) Spectroscopic properties and design of highly luminescent lanthanide coordination complexes. Coord Chem Rev 196:165–195
31. Bünzli J-CG (2015) On the design of highly luminescent lanthanide complexes. Coord Chem Rev 293–294:19–47
32. Bünzli JCG (2010) Lanthanide luminescence for biomedical analyses and imaging. Chem Rev 110:2729–2755
33. Cotton S (2005) Electronic and magnetic properties of the lanthanides. In: Lanthanide and actinide chemistry. Wiley, West Sussex. pp 61–83
34. Frison R, Cernuto G, Cervellino A et al (2013) Magnetite-maghemite nanoparticles in the 5-15 nm range: correlating the core-shell composition and the surface structure to the magnetic properties. A total scattering study. Chem Mater 25:4820–4827
35. Piao Y, Kim J et al (2008) Wrap–bake–peel process for nanostructural transformation from β-FeOOH nanorods to biocompatible iron oxide nanocapsules. Nat Mater 7:242–247

36. Prado Y, Daffé N, Michel A et al (2015) Enhancing the magnetic anisotropy of maghemite nanoparticles via the surface coordination of molecular complexes. Nat Commun 6:10139
37. Lacroix L, Lachaize S, Falqui A et al (2009) Iron nanoparticle growth in organic superstructures. J Am Chem Soc 131:549–557
38. Tadic M, Panjan M, Damnjanovic V, Milosevic I (2014) Magnetic properties of hematite (α-Fe_2O_3) nanoparticles prepared by hydrothermal synthesis method. Appl Surf Sci 320: 183–187
39. Lu Y, Lu X, Mayers BT et al (2008) Synthesis and characterization of magnetic Co nanoparticles: a comparison study of three different capping surfactants. J Solid State Chem 181:1530–1538
40. Peng S, Wang C, Xie J, Sun S (2006) Synthesis and stabilization of monodisperse Fe nanoparticles. J Am Chem Soc 128:10676–10677
41. Huber D (2005) Synthesis, properties, and applications of iron nanoparticles. Small 1: 482–501
42. Chen HM, Hsin CF, Chen PY et al (2009) Ferromagnetic $CoPt_3$ nanowires: structural evolution from fcc to ordered $L1_2$. J Am Chem Soc 131:15794–15801
43. Colak L, Hadjipanayis GC (2009) Chemically synthesized FePt nanoparticles with controlled particle size, shape and composition. Nanotechnology 20:485602
44. Ghosh Chaudhuri R, Paria S (2012) Core/shell nanoparticles: classes, properties, synthesis mechanisms, characterization, and applications. Chem Rev 112:2373–2433
45. Lu A-H, Salabas E, Schüth F (2007) Magnetic nanoparticles: synthesis, protection, functionalization, and application. Angew Chemie Int Ed 46:1222–1244
46. Hasany F, Ahmed S et al (2013) Systematic review of the preparation techniques of iron oxide magnetic nanoparticles. Nanosci Nanotechnol 2:148–158
47. Jolivet J-P, Chanèac C, Tronc E (2004) Iron oxide chemistry. From molecular clusters to extended solid networks. Chem Commun 5:481–483
48. Barbosa HP, Kai J, Silva IGN et al (2015) Luminescence investigation of R^{3+}-doped alkaline earth tungstates prepared by a soft chemistry method. J Lumin 170:1–7
49. Yi G, Lu H, Zhao S et al (2004) Synthesis, characterization, and biological application of size-controlled nanocrystalline $NaYF_4$:Yb,Er infrared-to-visible up-conversion phosphors. Nano Lett 4:2191–2196
50. Ximendes EC, Rocha U, Jacinto C et al (2016) Self-monitored photothermal nanoparticles based on core–shell engineering. Nanoscale 8:3057–3066
51. Gribanov NM, Bibik EE, Buzunov OV, Naumov VN (1990) Physico-chemical regularities of obtaining highly dispersed magnetite by the method of chemical condensation. J Magn Magn Mater 85:7–10
52. Boistelle R, Astier JP (1988) Crystallization mechanisms in solution. J Cryst Growth 90: 14–30
53. Knobel M, Nunes WC, Socolovsky LM et al (2008) Superparamagnetism and other magnetic features in granular materials: a review on ideal and real systems. J Nanosci Nanotechnol 8:2836–2857
54. Tresilwised N, Pithayanukul P, Plank C (2005) Factors affecting sizes of magnetic particles formed by chemical co-precipitation. Pharmacy Mahidol Ac Th 32:71–76
55. Kim DK, Zhang Y, Voit W et al (2001) Synthesis and characterization of surfactant-coated superparamagnetic monodispersed iron oxide nanoparticles. J Magn Magn Mater 225:30–36
56. Vayssières L, Chanéac C, Tronc E, Jolivet JP (1998) Size tailoring of magnetite particles formed by aqueous precipitation: an example of thermodynamic stability of nanometric oxide particles. J Colloid Interface Sci 205:205–212
57. Li Y, Afzaal M, O'Brien P (2006) The synthesis of amine-capped magnetic (Fe, Mn, Co, Ni) oxide nanocrystals and their surface modification for aqueous dispersibility. J Mater Chem 16:2175
58. Rockenberger J, Scher EC, Alivisatos AP (1999) A new nonhydrolytic single-precursor approach to surfactant-capped nanocrystals of transition metal oxides. J Am Chem Soc 121:11595–11596

59. Hyeon T (2003) Chemical synthesis of magnetic nanoparticles. Chem Commun 927–934
60. Chen X, Liu Y, Tu D (2014) Lanthanide-doped luminescent nanomaterials. Springer, Berlin
61. Mahalingam V, Vetrone F, Naccache R et al (2009) Colloidal Tm^{3+}/Yb^{3+}-doped $LiYF_4$ nanocrystals: multiple luminescence spanning the UV to NIR regions via low-energy excitation. Adv Mater 21:4025–4028
62. Chen G, Ohulchanskyy TY, Kumar R et al (2010) Ultrasmall monodisperse $NaYF_4$:Yb^{3+}/Tm^{3+} nanocrystals with enhanced near-infrared to near-infrared upconversion photoluminescence. ACS Nano 4:3163–3168
63. Naccache R, Vetrone F, Mahalingam V et al (2009) Controlled synthesis and water dispersibility of hexagonal phase $NaGdF_4$:Ho^{3+}/Yb^{3+} nanoparticles. Chem Mater 21:717–723
64. Liu Q, Sun Y, Yang T et al (2011) Sub-10 nm hexagonal lanthanide-doped $NaLuF_4$ upconversion nanocrystals for sensitive bioimaging in vivo. J Am Chem Soc 133:17122–17125
65. Vetrone F, Mahalingam V, Capobianco JA (2009) Near-infrared-to-blue upconversion in colloidal $BaYF_5$:Tm^{3+},Yb^{3+} nanocrystals. Chem Mater 21:1847–1851
66. Yang D, Li C, Li G et al (2011) Colloidal synthesis and remarkable enhancement of the upconversion luminescence of $BaGdF_5$:Yb^{3+}/Er^{3+} nanoparticles by active-shell modification. J Mater Chem 21:5923–5927
67. Yi G, Peng Y, Gao Z (2011) Strong red-emitting near-infrared-to-visible upconversion fluorescent nanoparticles. Chem Mater 23:2729–2734
68. Sun X, Zhang Y-W, Du Y-P et al (2007) From trifluoroacetate complex precursors to monodisperse rare-earth fluoride and oxyfluoride nanocrystals with diverse shapes through controlled fluorination in solution phase. Chem A Eur J 13:2320–2332
69. Sun S, Zeng H (2002) Size-controlled synthesis of magnetite nanoparticles. J Am Chem Soc 124:8204–8205
70. Brollo MEF, López-Ruiz R, Muraca D et al (2014) Compact $Ag@Fe_3O_4$ core-shell nanoparticles by means of single-step thermal decomposition reaction. Sci Rep 4:6839
71. Liz-Marzán LM, Kamat PV (2003) Nanoscale materials, 1st edn. Springer, New York
72. Langevin D (1992) Micelles and microemulsions. Annu Rev Phys Chem 43:341–369
73. Danielsson I, Lindman B (1981) The definltion of microemulsion. Colloids Surf 3:391–392
74. Malik MA, Wani MY, Hashim MA (2012) Microemulsion method: a novel route to synthesize organic and inorganic nanomaterials. Arab J Chem 5:397–417
75. Liu C, Zou B, Rondinone AJ, Zhang ZJ (2000) Reverse micelle synthesis and characterization of superparamagnetic $MnFe_2O_4$ spinel ferrite nanocrystallites. J Phys Chem B 104:1141–1145
76. Hashim M, Shirsath SE, Meena SS et al (2015) Manganese ferrite prepared using reverse micelle process: structural and magnetic properties characterization. J Alloys Compd 642:70–77
77. Dongale TD, Shinde SS, Kamat RK, Rajpure KY (2014) Nanostructured TiO_2 thin film memristor using hydrothermal process. J Alloys Compd 593:267–270
78. Xu H, Wang H, Zhang Y et al (2004) Hydrothermal synthesis of zinc oxide powders with controllable morphology. Ceram Int 30:93–97
79. Lee E, Kim Y, Heo J, Park K-M (2015) 3D metal–organic framework based on a lower-rim acid-functionalized calix[4]arene: crystal-to-crystal transformation upon lattice solvent removal. Cryst Growth Des 15:3556–3560
80. Wang X, Zhuang J, Peng Q, Li Y (2005) A general strategy for nanocrystal synthesis. Nature 437:121–124
81. Rabenau A (1985) The role of hydrothermal synthesis in preparative chemistry. Angew Chemie Int Ed 24:1026–1040
82. Einarsrud M-A, Grande T (2014) 1D oxide nanostructures from chemical solutions. Chem Soc Rev 43:2187–2199
83. Cai H, An X, Cui J et al (2013) Facile hydrothermal synthesis and surface functionalization of polyethyleneimine-coated iron oxide nanoparticles for biomedical applications. ACS Appl Mater Interfaces 5:1722–1731

84. Tong L, Shi J, Liu D, Li Q (2012) Luminescent and magnetic properties of Fe_3O_4@SiO_2@Y_2O_3:Eu^{3+} composites with core–shell structure. J Phys Chem C 116:7153–7157
85. Zhong C, Yang P, Li X et al (2012) Monodisperse bifunctional Fe_3O_4@$NaGdF_4$:Yb/Er@$NaGdF_4$:Yb/Er core–shell nanoparticles. RSC Adv 2:3194–3197
86. Zhang L, Wang Y-S, Yang Y et al (2012) Magnetic/upconversion luminescent mesoparticles of Fe_3O_4@LaF_3:Yb^{3+},Er^{3+} for dual-modal bioimaging. Chem Commun 48:11238–11240
87. Peng H, Liu G, Dong X et al (2012) Magnetic, luminescent and core–shell structured Fe_3O_4@YF_3:Ce^{3+},Tb^{3+} bifunctional nanocomposites. Powder Technol 215–216:242–246
88. Jie G, Yuan J (2012) Novel magnetic Fe_3O_4@CdSe composite quantum dot-based electrochemiluminescence detection of thrombin by a multiple DNA cycle amplification strategy. Anal Chem 84:2811–2817
89. Wang H, Sun L, Li Y et al (2011) Layer-by-layer assembled Fe_3O_4@C@CdTe core/shell microspheres as separable luminescent probe for sensitive sensing of Cu^{2+} ions. Langmuir 27:11609–11615
90. Yu X, Wan J, Shan Y et al (2009) A facile approach to fabrication of bifunctional magnetic-optical Fe_3O_4@ZnS microspheres. Chem Mater 21:4892–4898
91. Gu H, Zheng R, Zhang X, Xu B (2004) Facile one-pot synthesis of bifunctional heterodimers of nanoparticles: a conjugate of quantum dot and magnetic nanoparticles. J Am Chem Soc 126:5664–5665
92. Liu G, Peng H, Wang J, Dong X (2012) Fe_3O_4@GdF_3:Er^{3+},Yb^{3+} nanoparticles: synthesis and bifunctional properties. J Optoelectron Adv Mater 14:205–209
93. Wu T, Pan H, Chen R et al (2016) Effect of solution pH value changes on fluorescence intensity of magnetic-luminescent Fe_3O_4@Gd_2O_3:Eu^{3+} nanoparticles. J Rare Earths 34:71–76
94. He H, Xie MY, Ding Y, Yu XF (2009) Synthesis of Fe_3O_4@LaF_3:Ce,Tb nanocomposites with bright fluorescence and strong magnetism. Appl Surf Sci 255:4623–4626
95. Atabaev T, Kim H-K, Hwang Y-H (2013) Fabrication of bifunctional core-shell Fe_3O_4 particles coated with ultrathin phosphor layer. Nanoscale Res Lett 8:357
96. Yu X, Shan Y, Li G, Chen K (2011b) Synthesis and characterization of bifunctional magnetic–optical Fe_3O_4@SiO_2@Y_2O_3:Yb^{3+},Er^{3+} near-infrared-to-visible up-conversion nanoparticles. J Mater Chem 21:8104–8109
97. Wu A, Zhang Z (2015) Luminescent and magnetic properties of carbon-based $FeYO_3$/Y_2O_3:Eu^{3+} nanocomposites. Appl Surf Sci 356:1077–1081
98. Bi F, Dong X, Wang J, Liu G (2014) Coaxial electrospinning preparation and properties of magnetic–photoluminescent bifunctional $CoFe_2O_4$@Y_2O_3:Eu^{3+} coaxial nanofibers. J Mater Sci Mater Electron 25:4259–4267
99. Peng H, Liu G, Dong X et al (2011) Preparation and characteristics of Fe_3O_4@YVO_4:Eu^{3+} bifunctional magnetic–luminescent nanocomposites. J Alloys Compd 509:6930–6934
100. Sun P, Zhang H, Liu C et al (2010) Preparation and characterization of Fe_3O_4/CdTe magnetic/fluorescent nanocomposites and their applications in immuno-labeling and fluorescent imaging of cancer cells. Langmuir 26:1278–1284
101. Du GH, Liu ZL, Lu QH et al (2006) Fe_3O_4/CdSe/ZnS magnetic fluorescent bifunctional nanocomposites. Nanotechnology 17:2850–2854
102. Shen J, Sun L-D, Zhang Y-W, Yan C-H (2010) Superparamagnetic and upconversion emitting Fe_3O_4/$NaYF_4$:Yb,Er hetero-nanoparticles via a crosslinker anchoring strategy. Chem Commun 46:5731–5733
103. Fang J, Saunders M, Guo Y et al (2010) Green light-emitting $LaPO_4$:Ce^{3+}:Tb^{3+} koosh nanoballs assembled by p-sulfonato-calix[6]arene coated superparamagnetic Fe_3O_4. Chem Commun 46:3074–3076
104. Zhu H, Tao J, Wang W et al (2013) Magnetic, fluorescent, and thermo-responsive Fe_3O_4/rare earth incorporated poly(St-NIPAM) core–shell colloidal nanoparticles in multimodal optical/magnetic resonance imaging probes. Biomaterials 34:2296–2306

105. Zhu H, Shang Y, Wang W et al (2013) Fluorescent magnetic Fe_3O_4/rare earth colloidal nanoparticles for dual-modality imaging. Small 9:2991–3000
106. Barick KC, Sharma A, Shetake NG et al (2015) Covalent bridging of surface functionalized Fe_3O_4 and YPO_4:Eu nanostructures for simultaneous imaging and therapy. Dalt Trans 44:14686–14696
107. Parchur AK, Ansari AA, Singh BP et al (2014) Enhanced luminescence of $CaMoO_4$:Eu by core@shell formation and its hyperthermia study after hybrid formation with Fe_3O_4: cytotoxicity assessment on human liver cancer cells and mesenchymal stem cells. Integr Biol 6:53–64
108. Ye F, Barrefelt Å, Asem H et al (2014) Biodegradable polymeric vesicles containing magnetic nanoparticles, quantum dots and anticancer drugs for drug delivery and imaging. Biomaterials 35:3885–3894
109. Hong X, Li J, Wang M et al (2004) Fabrication of magnetic luminescent nanocomposites by a layer-by-layer self-assembly approach. Chem Mater 16:4022–4027
110. Gaponik N, Radtchenko IL, Sukhorukov GB, Rogach AL (2004) Luminescent polymer microcapsules addressable by a magnetic field. Langmuir 20:1449–1452
111. Wang D, He J, Rosenzweig N, Rosenzweig Z (2004) Superparamagnetic Fe_2O_3 beads−CdSe/ZnS quantum dots core−shell nanocomposite particles for cell separation. Nano Lett 4:409–413
112. Chen O, Riedemann L, Etoc F et al (2014) Magneto-fluorescent core-shell supernanoparticles. Nat Commun 5:5093
113. Yang J, Lim E-K, Lee HJ et al (2008) Fluorescent magnetic nanohybrids as multimodal imaging agents for human epithelial cancer detection. Biomaterials 29:2548–2555
114. Gallagher JJ, Tekoriute R, O'Reilly J-A et al (2009) Bimodal magnetic-fluorescent nanostructures for biomedical applications. J Mater Chem 19:4081–4084
115. Yuet KP, Hwang DK, Haghgooie R, Doyle PS (2010) Multifunctional superparamagnetic janus particles. Langmuir 26:4281–4287
116. Kaewsaneha C, Bitar A, Tangboriboonrat P et al (2014) Fluorescent-magnetic Janus particles prepared via seed emulsion polymerization. J Colloid Interface Sci 424:98–103
117. Chekina N, Horák D, Jendelová P et al (2011) Fluorescent magnetic nanoparticles for biomedical applications. J Mater Chem 21:7630–7639
118. Ge Y, Zhang Y, He S et al (2009) Fluorescence modified chitosan-coated magnetic nanoparticles for high-efficient cellular imaging. Nanoscale Res Lett 4:287–295
119. Torkpur-Biglarianzadeh M, Salami-Kalajahi M (2015) Multilayer fluorescent magnetic nanoparticles with dual thermoresponsive and pH-sensitive polymeric nanolayers as anticancer drug carriers. RSC Adv 5:29653–29662
120. Lim E-K, Yang J, Dinney CPN et al (2010) Self-assembled fluorescent magnetic nanoprobes for multimode-biomedical imaging. Biomaterials 31:9310–9319
121. Kaewsaneha C, Opaprakasit P, Polpanich D et al (2012) Immobilization of fluorescein isothiocyanate on magnetic polymeric nanoparticle using chitosan as spacer. J Colloid Interface Sci 377:145–152
122. Stöber W, Fink A, Bohn E (1968) Controlled growth of monodisperse silica spheres in the micron size range. J Colloid Interface Sci 26:62–69
123. Santra S, Tapec R, Theodoropoulou N et al (2001) Synthesis and characterization of silica-coated iron oxide nanoparticles in microemulsion: the effect of nonionic surfactants. Langmuir 17:2900–2906
124. Pogorilyi RP, Melnyk IV, Zub YL et al (2014) New product from old reaction: uniform magnetite nanoparticles from iron-mediated synthesis of alkali iodides and their protection from leaching in acidic media. RSC Adv 4:22606–22612
125. Yu S-Y, Zhang H-J, Yu J-B et al (2007) Bifunctional magnetic-optical nanocomposites: grafting lanthanide complex onto core-shell magnetic silica nanoarchitecture. Langmuir 23:7836–7840

126. Yu S, Fu L, Zhou Y, Su H (2011) Novel bifunctional magnetic-near-infrared luminescent nanocomposites: near-infrared emission from Nd and Yb. Photochem Photobiol Sci 10:548–553
127. Spaldin NA (2010) Magnetic materials. Fundamentals and applications. Cambridge University Press, New York
128. Kurzen H, Bovigny L, Bulloni C, Daul C (2013) Electronic structure and magnetic properties of lanthanide 3+ cations. Chem Phys Lett 574:129–132
129. Van Vleck JH (1978) Quantum mechanics-key understanding magnetism. Rev Mod Phys 50:181–189
130. Bünzli J-CG, Piguet C (2005) Taking advantage of luminescent lanthanide ions. Chem Soc Rev 34:1048–1077
131. Dorenbos P (2002) Light output and energy resolution of Ce^{3+}-doped scintillators. Nucl Instrum Methods Phys Res A 486:208–213
132. Binnemans K (2015) Interpretation of europium(III) spectra. Coord Chem Rev 295:1–45
133. Xu W, Park JY, Kattel K et al (2012) A T_1, T_2 magnetic resonance imaging (MRI)-fluorescent imaging (FI) by using ultrasmall mixed gadolinium–europium oxide nanoparticles. New J Chem 36:2361–2367
134. Li C, Li YX, Law GL et al (2006) Fast water-exchange Gd^{3+}-(DO3A-like) complex functionalized with Aza-15-crown-5 showing prolonged residence lifetime in vivo. Bioconjug Chem 17:571–574
135. Szczeszak A, Ekner-Grzyb A, Runowski M et al (2015) Synthesis, photophysical analysis, and in vitro cytotoxicity assessment of the multifunctional (magnetic and luminescent) core@shell nanomaterial based on lanthanide-doped orthovanadates. J Nanopart Res 17:143
136. Hu C, Xia T, Gong Y et al (2016) Emulsifier-free emulsion polymerized poly(MMA-HEMA-$Eu(AA)_3$Phen)/Fe_3O_4 magnetic fluorescent bifunctional nanospheres for magnetic resonance and optical imaging. Chinese J Polym Sci 34:135–146
137. Xia A, Gao Y, Zhou J et al (2011) Core-shell $NaYF_4$:Yb^{3+},Tm^{3+}@Fe_xO_y nanocrystals for dual-modality T_2-enhanced magnetic resonance and NIR-to-NIR upconversion luminescent imaging of small-animal lymphatic node. Biomaterials 32:7200–7208
138. Zhu X, Zhou J, Chen M et al (2012) Core–shell Fe_3O_4@$NaLuF_4$:Yb,Er/Tm nanostructure for MRI, CT and upconversion luminescence tri-modality imaging. Biomaterials 33:4618–4627
139. Guo R, Wang J, Dong X et al (2014) A new tactics to fabricate flexible nanobelts with enhanced magnetic-luminescent bifunction. J Mater Sci Mater Electron 25:2561–2568
140. Leyu W, Zhihua Y, Yi Z, Lun W (2009) Bifunctional nanoparticles with magnetization and luminescence. J Phys Chem C 113:3955–3959
141. Li B, Fan H, Zhao Q, Wang C (2016) Synthesis, characterization and cytotoxicity of novel multifunctional Fe_3O_4@SiO_2@$GdVO_4$:Dy^{3+} core-shell nanocomposite as a drug carrier. Materials 9:149
142. Sukumar UK, Bhushan B, Dubey P et al (2013) Emerging applications of nanoparticles for lung cancer diagnosis and therapy. Int Nano Lett 3:1–17
143. Runowski M, Lis S (2015) Synthesis, surface modification/decoration of luminescent–magnetic core/shell nanomaterials, based on the lanthanide doped fluorides (Fe_3O_4/SiO_2/NH_2/PAA/LnF_3). J Lumin 170:484–490
144. Sonuga-Barke E, Brandeis D, Cortese S et al (2013) Response to Chronis-Tuscano et al. and Arns and Strehl. Am J Psychiatry 170:800–802
145. Roland S, Thomas W, Yitzhak R et al (1957) Targeted magnetic hyperthermia. Ther Deliv 2:815–838
146. Walter A, Billotey C, Garofalo A et al (2014) Mastering the shape and composition of dendronized iron oxide nanoparticles to tailor magnetic resonance imaging and hyperthermia. Chem Mater 26:5252–5264
147. Lepock JR (2003) Cellular effects of hyperthermia: relevance to the minimum dose for thermal damage. Int J Hyperth 19:252–266

148. Xie J, Zhang Y, Yan C et al (2014) High-performance PEGylated Mn-Zn ferrite nanocrystals as a passive-targeted agent for magnetically induced cancer theranostics. Biomaterials 35:9126–9136
149. Thrall DE, Larue SM, Pruitt AF et al (2006) Changes in tumour oxygenation during fractionated hyperthermia and radiation therapy in spontaneous canine sarcomas. Int J Hyperth 22:365–373
150. Gazeau F, Lévy M, Wilhelm C (2008) Optimizing magnetic nanoparticle design for nanothermotherapy. Nanomedicine (Lond) 3:831–844
151. Luwang MN, Chandra S, Bahadur D, Srivastava SK (2012) Dendrimer facilitated synthesis of multifunctional lanthanide based hybrid nanomaterials for biological applications. J Mater Chem 22:3395–3403
152. Singh LP, Singh NP, Srivastava SK (2015) Terbium doped SnO_2 nanoparticles as white emitters and SnO_2:5Tb/Fe_3O_4 magnetic luminescent nanohybrids for hyperthermia application and biocompatibility with HeLa cancer cells. Dalt Trans 44:6457–6465
153. Prasad AI, Parchur AK, Juluri RR et al (2013) Bi-functional properties of Fe_3O_4@YPO_4:Eu hybrid nanoparticles: hyperthermia application. Dalton Trans 42:4885–4896
154. Kempe H, Kates SA, Kempe M (2011) Nanomedicine's promising therapy: magnetic drug targeting. Expert Rev Med Devices 8:291–294
155. Marcu A, Pop S, Dumitrache F et al (2013) Magnetic iron oxide nanoparticles as drug delivery system in breast cancer. Appl Surf Sci 281:60–65
156. Hola K, Markova Z, Zoppellaro G et al (2015) Tailored functionalization of iron oxide nanoparticles for MRI, drug delivery, magnetic separation and immobilization of biosubstances. Biotechnol Adv 33:1162–1176
157. Mohapatra S, Rout SR, Das RK et al (2016) Highly hydrophilic luminescent magnetic mesoporous carbon nanospheres for controlled release of anticancer drug and multimodal imaging. Langmuir 32:1611–1620
158. Bao Y, Wen T, Samia ACS et al (2015) Magnetic nanoparticles: material engineering and emerging applications in lithography and biomedicine. J Mater Sci 51:513–553
159. Wan Q, Xie L, Gao L et al (2013) Self-assembled magnetic theranostic nanoparticles for highly sensitive MRI of minicircle DNA delivery. Nanoscale 5:744–752
160. Wang C, Cheng L, Liu Z (2011) Drug delivery with upconversion nanoparticles for multifunctional targeted cancer cell imaging and therapy. Biomaterials 32:1110–1120
161. Gambhir SS, Weiss S (2005) Quantum dots for live cells, in vivo imaging, and diagnostics. Science 307:538–544
162. Xu H, Cheng L, Wang C et al (2011) Polymer encapsulated upconversion nanoparticle/iron oxide nanocomposites for multimodal imaging and magnetic targeted drug delivery. Biomaterials 32:9364–9373
163. Singh RK, Patel KD, Kim JJ et al (2014) Multifunctional hybrid nanocarrier: magnetic CNTs ensheathed with mesoporous silica for drug delivery and imaging system. ACS Appl Mater Interfaces 6:2201–2208
164. Snyder P, Joshi A, Serna JD (2014) Modeling a nanocantilever-based biosensor using a stochastically perturbed harmonic oscillator. Int J Nanosci 13:1450011
165. Justino CIL, Rocha-Santos TAP, Cardoso S et al (2013) Strategies for enhancing the analytical performance of nanomaterial-based sensors. TrAC Trends Anal Chem 47:27–36
166. Haun JB, Yoon T-J, Lee H, Weissleder R (2010) Magnetic nanoparticle biosensors. Wiley Interdiscip Rev Nanomed Nanobiotechnol 2:291–304
167. Arvand M, Hassannezhad M (2014) Magnetic core-shell Fe_3O_4@SiO_2/MWCNT nanocomposite modified carbon paste electrode for amplified electrochemical sensing of uric acid. Mater Sci Eng C 36:160–167
168. Teymourian H, Salimi A, Khezrian S (2013) Fe_3O_4 magnetic nanoparticles/reduced graphene oxide nanosheets as a novel electrochemical and bioeletrochemical sensing platform. Biosens Bioelectron 49:1–8
169. Dou Q, Idris NM, Zhang Y (2013) Sandwich-structured upconversion nanoparticles with tunable color for multiplexed cell labeling. Biomaterials 34:1722–1731

170. Nichkova M, Dosev D, Gee SJ et al (2005) Microarray immunoassay for phenoxybenzoic acid using polymer encapsulated Eu:Gd_2O_3 nanoparticles as fluorescent labels. Anal Chem 77:6864–6873
171. Shen J, Sun LD, Zhu JD et al (2010b) Biocompatible bright YVO_4:Eu nanoparticles as versatile optical bioprobes. Adv Funct Mater 20:3708–3714
172. Idris NM, Li Z, Ye L et al (2009) Tracking transplanted cells in live animal using upconversion fluorescent nanoparticles. Biomaterials 30:5104–5113
173. Niedbala RS, Feindt H, Kardos K et al (2001) Detection of analytes by immunoassay using up-converting phosphor technology. Anal Biochem 293:22–30
174. Deng R, Xie X, Vendrell M et al (2011) Intracellular glutathione detection using MnO_2-nanosheet-modified upconversion nanoparticles. J Am Chem Soc 133:20168–20171